Reflectance spectroscopy (0.3–2.5 μm) at various scales for bulk-rock identification

Maria Sgavetti
Loredana Pompilio
Sandro Meli
Università degli Studi di Parma, Dipartimento di Scienze della Terra, Parco Area delle Scienze, 157/A, 43100 Parma, Italy

ABSTRACT

We discussed the possibilities and open questions concerning laboratory reflectance spectroscopy, spectroscopic measurements in the field, hyperspectral image data from spacecraft, and integration of multiscale data. Open questions included: (1) bulk-rock spectral complexity, which provides the geologic basis for every spectroscopic analysis; (2) criteria for laboratory and field spectra classification, as a tool for (3) end-member selection for image data classification; (4) peculiar spectral characteristics of Mount Etna basalts; and (5) effects of remote-sensing data quality. The last three items emerged during a multiscale survey on the Mount Etna volcano.

Our laboratory spectroscopic analyses, supported by specific petrographic analyses, showed the relationship between absorption-band frequency and spectrally active functional groups and the unexpected effects of bulk-rock composition on this relationship. We studied the muscovite Al-OH band in quartzite and micaschist and Fe^{2+} band in pyroxene-bearing cumulates.

Laboratory reflectance spectra of rocks were classified using the concept of spectrofacies. In the case of metamorphic rocks, the result was a tree-structure of rock spectral classes mainly based on the predominant vibrational processes. In the case of basalts, characterized by an overall similarity in their composition, the classes were determined on the basis of overall shape of the spectral curve and on electronic process intensities. Here, we report first results of multiscale data integration for the Mount Etna volcano. Etna rocks consist of basalts, with very low albedo and variable degrees of alteration, and recent lava flows are characterized by overall low reflectance in both ASTER (advanced spaceborne thermal emission and reflection radiometer) and Hyperion color-composite images. We carried out Spectral Angle Mapper (SAM) classification of Hyperion images, where individual field spectra represented suitable end members for classification of recent lava and pyroclastic deposits. We used field spectra linear combinations to classify mixed pixels and to approximate the classification of altered and oxidized effusive products. Only two laboratory spectral classes coincided with field spectra classes; laboratory spectra were mainly used for spectral features attribution. The overall spectral shape of some of these spectra is still under study. Noise level in Hyperion data precluded the identification of subtle diagnostic iron absorption bands.

Keywords: reflectance spectra, rocks, laboratory studies, surface, Hyperion satellite.

INTRODUCTION

Spectroscopy at various scales is used here to mean spectroscopic measurements in experimental conditions characterized by different observational distances. According to the instantaneous field of view (IFOV), the increase of sensor-target distance causes lower at-sensor irradiance with a consequent decrease of the signal-to-noise ratio. As a consequence, ground and/or spectral resolutions are degraded, and the probability of both spectral inhomogeneity within the pixel and ambiguity in spectral interpretation increases.

Variation of the observational distance and consequent data degradation also control the data resolution threshold for surface complexity analysis. Surface complexity manifests on different scales. The macro-complexity is due to topographic effects. It produces lightning and radiance variations among the pixels and is not considered in this paper. The meso-complexity occurs at subpixel scale, including surface texture and mixed pixels. Surface texture is the object of recent theoretical studies on the reflectance distribution function (e.g., Hapke, 2001). The reflectance of a mixed pixel is generally assumed to result in a linear combination of the spectral properties of the component materials, proportionally to their areal distribution within the pixel. In agreement with this assumption, meso-complexity is not further discussed here. The micro-complexity is intrinsic to the surface individual lithologies. It derives from the fact that the rocks are formed by many minerals with different chemistries intimately mixed together. In addition, several rock-forming minerals with similar chemistries have distinct crystal structures and a variety of grain sizes arranged into a number of rock textural patterns. All of these micro-complexity variables affect bulk-rock spectral properties at different observational scales.

The micro-complexity of rocks is commonly analyzed with laboratory spectroscopy. However, hyperspectral imaging spectrometers are supposed to be suitable for investigating rock micro-complexity from remote distances, in spite of some problems due to low signal-to-noise ratios. Imaging interferometers recently developed for remote-sensing purposes operate using the whole at sensor radiance (e.g., Meigs et al., 1997; Barducci et al., 2004), thus increasing both signal-to-noise ratios and spatial and spectral resolutions with respect to the optical dispersion systems. Such improved performances allow remotely sensed data to be reasonably compared to field and laboratory data, opening up new chances for resolving the micro-complexity of the surface.

The purpose of hyperspectral remote-data analysis is to identify and map different targets: (1) chemical species, such as Fe and Ti distribution on a planetary surface (e.g., Wilcox et al., 2005); (2) local abundances of minerals, for example, olivine and pyroxene amount in soils on Mars (e.g., Mustard et al., 2005); and (3) nature and areal distribution of rocks for

Geosphere; May 2006; v. 2; no. 3; p. 142–160; doi: 10.1130/GES00039.1; 13 figures, 8 tables.

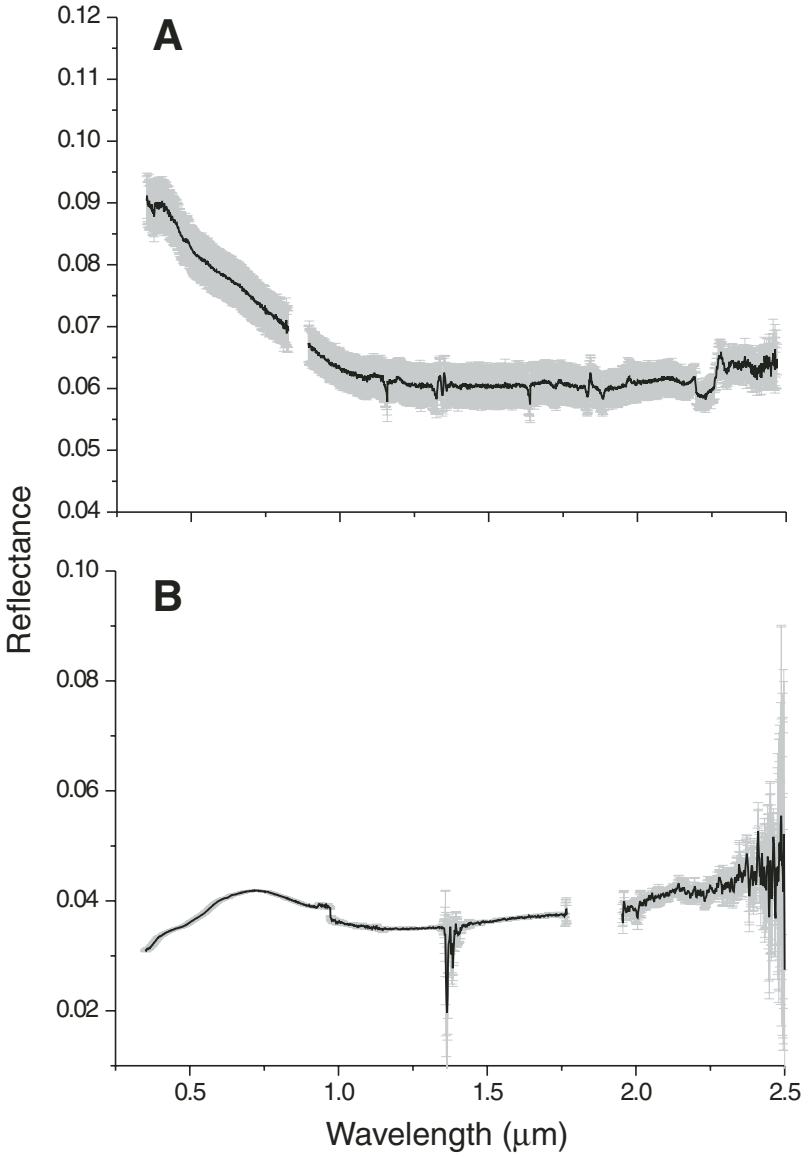

Figure 1. (A) Average spectrum of 10 laboratory measurements randomly distributed on the slab surface of the sample (Mount Etna recent lava); gray area represents the standard deviation. (B) Average spectrum of 5 in situ measurements acquired on a target (Mount Etna pyroclastics); gray area represents the total uncertainty of measurements relative to the target.

local or regional studies (e.g., McSween et al., 2003). In the last case, all the factors contributing to bulk-rock spectral complexity should be taken into consideration in the choice of the end members for the remote-data classification. The most suitable end members should therefore be laboratory bulk-rock spectra, and appropriate criteria of analysis and classification of these spectra should be applied in order to synthesize and rank the diagnostic spectral characteristics.

On the other hand, accurate models for the interpretation of the bulk-rock spectral properties have not yet been fully established. Therefore, in a discussion about multiscale spectroscopy of bulk rocks, both the state of the art in understanding the spectral properties of a rock system as a whole, and the capability of remote sensing to resolve rock subtle spectral features should be considered (Sgavetti et al., 2006).

The purpose of this paper is to contribute to the general understanding of bulk-rock spectral properties for compositional analysis, classification, and mapping of data acquired in different experimental conditions. The discussion focuses on (1) the analysis of rock spectral variability, which is a component of the micro-complexity, in order to establish relationships between mineral chemistry and absorption bands in bulk-rock spectra, focusing on rock sequences that formed according to a given geologic process; this provides the geologic basis for every spectroscopic analysis, regardless of resolution and observational distance; (2) the criteria for bulk-rock spectral classification, which represents the necessary link between laboratory and remote-sensing spectroscopy; and (3) the problems arising when data from laboratory, in situ, and remote measurements are integrated; some of these problems emerged from the preliminary results of a multiscale survey in a particularly critical area characterized by an extremely low reflectance.

The spectral range investigated here is the 0.3–2.5 micron comprising near ultraviolet, visible and near infrared (UV-VIS-NIR) regions. Within this interval, electronic transitions and vibrational overtones are particularly sensitive to the chemical composition of several rock-forming minerals (e.g., Hunt, 1980).

DATA ACQUISITION

We measured the reflectance spectra of both slightly polished slab surfaces and particulate samples using a double-beam, double-monochromator spectrophotometer (Perkin-Elmer, Mod. λ19) equipped with a 60 mm integrating sphere internally covered by gold. The reflectance spectra were acquired between 0.35 and 2.50 μm, using a halogen lamp as radiation source. Calibration was performed with plates of Spectralon®. The measurements were performed in directional-hemispherical reflectance geometry, at room temperature and normal atmospheric pressure, with a spectral sampling of 1 nm. The spectrometer system incorporated a dual-background correction function, which automatically corrected the background absorptions. The resolution of the spectrophotometer was ±0.2 nm and ±0.8 nm for the UV/VIS and NIR ranges, respectively. The average spectra after 10 measurements per each sample were considered as representative of rock modal composition (Fig. 1A). The spectrometer was available at the spectroscopy laboratory of IFAC (Istituto di Fisica Applicata Nello Carrara), Consiglio Nazionale delle Ricerche (CNR), Florence, Italy.

In situ measurements were made using an ASD FieldSpec Pro FR portable spectrometer operating in the 0.35–2.50 μm spectral range (Sgavetti et al., 2003). Calibration was performed with plates of Spectralon®. The spectrometer was equipped with 1.4 m optic cable, 25° full angle cone of acceptance; the acquisition speed was 10 spectra/s. For each target, 1 s time of acquisition was adopted. Up to 5 acquisitions were averaged for each target within a site,

and are referred to as "spectrum" in the following (Fig. 1B). Field spectra were acquired with nadir geometry on surfaces with inclination up to 10°, from an average distance of 70 cm. A set of spectra of pyroclastic deposits was measured from a distance of 30 cm using a tripod.

ASTER (advanced spaceborne thermal emission and reflection radiometer) and Hyperion daytime images used for remote spectral analyses were acquired on 19 July 2003 and were provided by the INGV (Istituto Nazionale di Geofisica e Vulcanologia), Rome division. ASTER is a multispectral imager on board the National Aeronautics and Space Administration's (NASA) Terra spacecraft (http://asterweb.jpl.nasa.gov/). It covers a wide spectral region with 14 bands from the visible to the thermal infrared with high spatial, spectral, and radiometric resolution. An additional backward-looking near-infrared band provides stereo coverage. Spatial resolution and spectral bandpass vary with wavelength (Table 1). Hyperion is a hyperspectral imaging spectrometer on board NASA's EO-1 spacecraft (http://eo1.gsfc.nasa.gov/Technology/Hyperion.html). Hyperion produces spectra using 226 channels covering the range 0.4–2.4 μm with a spatial resolution of 30 m per pixel (Table 1). The Mount Etna ASTER and Hyperion overflights were accomplished under the supervision of M.F. Buongiorno, INGV, Rome.

Images of the multispectral Thematic Mapper sensor (TM) onboard Landsat 5 spacecraft (http://landsat.usgs.gov/index.php) were also used for a portion of the metamorphic basement of central Madagascar. TM has six bands in the 0.4–2.5 μm range and one in the 10–12 μm spectral ranges, with variable spectral and spatial resolutions, as shown in Table 1.

MICRO-COMPLEXITY AND ROCK SPECTRAL VARIABILITY

Several parameters, such as mineral chemistry and structure, grain size, and rock texture, contribute to the surface micro-complexity and affect the spectral properties of rocks. Variation in these parameters can produce both systematic and nonsystematic rock spectral variability. In this section, the spectroscopic variability and the effects of bulk-rock parameters are analyzed for igneous and metamorphic rocks, which form large portions of Earth's crust.

Bulk-Rock Spectroscopic Variability in Genetically Related Rocks

The diagnostic absorption features occurring in mineral and rock spectra are due to energy-matter interactions within molecular groups. The frequency of the quantic transitions between energy levels is peculiar to each individual absorption process and can have a range of variation, depending on both the chemical composition and crystal structure of minerals.

Metamorphism results from physical transformations and chemical reactions involving the original protolith, strictly controlled by pressure, temperature, and time. Protolith chemical composition, grain size, texture, and the nature of the circulating fluids also control the chemistry, mineralogy, and texture of metamorphic rocks. A sequence of metamorphic mineral assemblages associated in space indicates the range of metamorphic grade through an area.

Igneous rock-forming minerals primarily derive from fractional crystallization of a melt produced by mantle fusion and/or crustal assimilation, according to known sequences of processes. Main input variables are the composition of melt, temperature, pressure, oxygen, water, and gas fugacities. The output consists of series of mineral phases, some of which are solid solutions between two end members. A magmatic rock is therefore a complex chemical system, constrained by specific physic-chemical conditions that affect its composition, crystal structure, crystallinity degree, and texture.

Rock petrology and geochemistry resulting from different geologic processes affect the rock spectral signature. Hence, the spectral variability is intrinsic to the involved rock-forming process, whatever it is. As a result, genetically related rocks can display systematic variations of spectral parameters as functions of systematic variations of petrographical and geochemical parameters.

Spectroscopic Variability of Metamorphic and Mafic Intrusive Rocks

It has been shown that vibrational overtones of the fundamental Al-OH bond dominate the wavelength interval between 2.0 and 2.5 μm in spectra of phyllosilicate from rock types belonging to different geologic settings (e.g., Swayze et al., 1992; Duke, 1994; Longhi et al., 2001, 2004). The variation of Al-OH overtone band frequency as a function of the Al/Fe ratio has been observed for micas with several different compositions (Post and Noble, 1993), including hydrothermal muscovite (Swayze et al., 1992). A negative correlation has been independently observed by different researchers between the Al-OH overtone band centers and the octahedral Al content of muscovite, occurring both in metamorphosed graywackes from Black Hills, South Dakota (Duke, 1994), and in suites of quartzites and micaschists from the pre-Paleozoic basement of central Madagascar (Longhi et al., 2000, 2004), as shown in Figure 2A. The systematic shift toward shorter wavelengths of Al-OH overtone band centers as the $^{[VI]}$Al abundance increases in muscovite has been correlated with the increasing metamorphic grade. In one case, the metamorphic grade shifts from the biotite zone toward the sillimanite + K-feldspar zone (Black Hills graywacke; Duke, 1994); in the other, from the diopside zone toward the sillimanite + K-feldspar zone (central Madagascar quartzites and micaschists; Moine, 1974). The increasing grade of metamorphism is responsible for the progressive $^{[VI]}$Al enrichment in muscovite, according to progressively reduced phengite substitution within Al-undersaturated rocks (Guidotti and Sassi, 1976).

TABLE 1. CHARACTERISTICS OF THE THREE SENSOR SYSTEMS*

Sensor	Spectral range (μm)	Number of bands	Spectral resolution (μm)	Spatial resolution (m)	Swath width (km)
TM	0.40–2.40	6	0.060–0.270 variable	30	185.0
ASTER nadir mode	0.52–0.86†	3†	0.060–0.080† variable	15†	60.0
	1.60–2.43§	6§	0.045–0.100§ variable	30§	
Hyperion	0.40–2.50	220	0.010	30	7.5

Note: Landsat 5 Thematic Mapper (TM) data on Madagascar were acquired on 17 November 1990, at 9:12:00 local time. Advanced spaceborne thermal emission and reflection radiometer (ASTER) and Hyperion data were acquired on Mount Etna on 19 July 2003, at 10:52:00 and 10:25:00 local time, respectively.

*Parameters refer to the data used for this study.

†ASTER VNIR (visible near-infrared) subsystem.

§ASTER SWIR (short-wavelength infrared) subsystem.

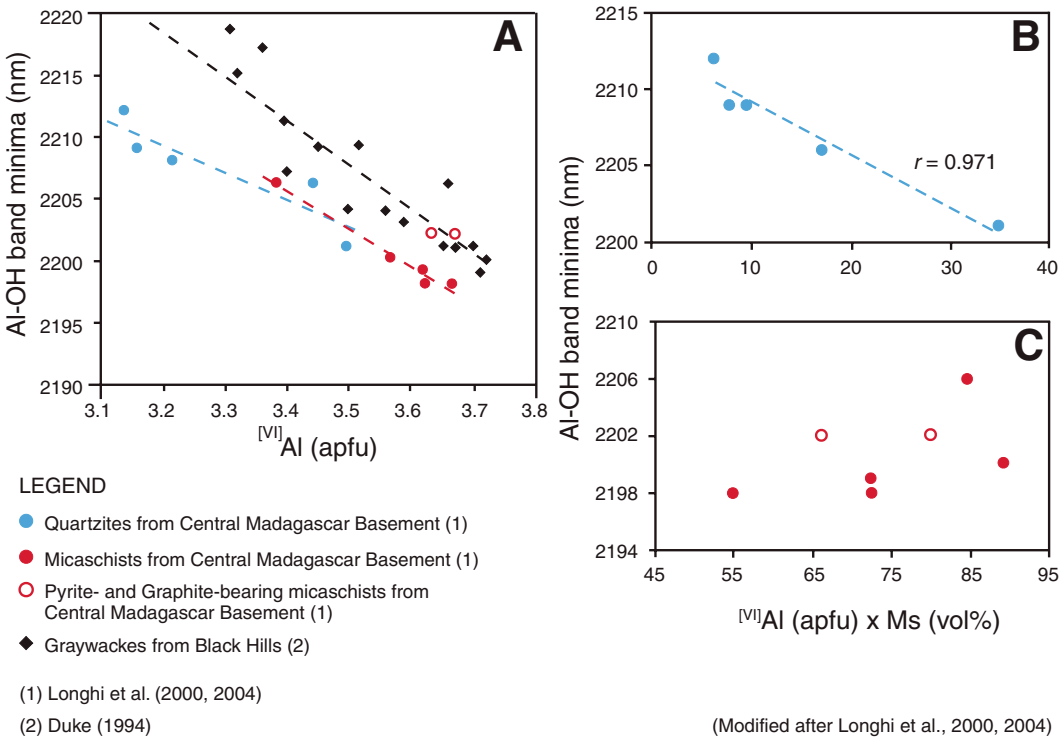

(Modified after Longhi et al., 2000, 2004)

Figure 2. (A) Inverse linear relationship between the Al-OH band wavelength and the ^{VI}Al abundance (apfu: atoms per formula unit), relative to muscovite in the quartzites-micaschists and graywackes suites. (B) Relationship between Al-OH band wavelength and ^{VI}Al abundance in muscovite times modal muscovite in quartzites; *r* is the coefficient of correlation. (C) Plot of Al-OH band wavelength and ^{VI}Al abundance in muscovite times modal muscovite in micaschists, showing the lack of any relationship. See discussion in the text.

In Figure 2A, the quartzite-micaschists and graywacke suites form distinct clusters in the $^{[VI]}$Al abundance versus Al-OH band center space. This was attributed to differing bulk-rock compositions (Longhi et al., 2000). In more detail, two slightly different variation trends also characterize the quartzite and micaschist distributions. The bulk-rock effect was analyzed considering the product of $^{[VI]}$Al (apfu: atoms per formula unit) times modal muscovite, which estimates the distribution of the spectroscopically active group within the rock. As shown in Figure 2B, the relationship between Al-OH overtone band centers and this distribution parameter is still negative (at a confidence level of 99%) in the case of quartzites, analogous to the relationship in Figure 2A. On the contrary, the two variables are not correlated for micaschists (Fig. 2C). This is consistent with the different bulk compositions, because the quartzites are composed of quartz with a small content of muscovite and tourmaline, while the micaschists consist of quartz, muscovite, biotite, and albite in various amounts.

Spectral variability was also observed for diagnostic absorptions due to electronic processes in iron-bearing minerals occurring in mafic rocks. Crystal field (CF) transitions in Fe^{2+}, preferentially when located in distorted octahedral crystallographic sites, commonly occur in ferromagnesian minerals such as olivine and pyroxene (Burns, 1993). The wavelength position of the resulting absorption bands has been accurately measured by several researchers, using sets of minerals containing different amounts of Fe, and calibration curves have been developed. Calibration curves are useful tools for quantitative analysis of such minerals, especially for remote spectroscopy of rocks (Cloutis and Gaffey, 1991).

This well-demonstrated experimental basis was used here to study the spectral behavior of a suite of cumulates (mainly norites and anorthosites) belonging to the Bjerkreim-Sokndal Layered Intrusion (Norway). Their composition varied within each megacyclic unit and even within sublayers. The rock modal composition mainly included plagioclase, ilmenite, and Ca-poor pyroxene. The absorption bands diagnostic of pyroxene near 0.9 and 1.8 µm dominated the rock slab surface spectra. Accurate electron microprobe and Mössbauer analyses supported the attribution of the observed bands to Fe^{2+}/M2 site crystal field transitions. Throughout the whole set of samples, absorption band minima shifted toward longer wavelengths with increasing Fe^{2+} content in octahedral M2 sites (Fig. 3A), which is consistent with the measurements derived from spectra of pyroxene separates from the same rock set (Pompilio, 2005a, 2005b) and in agreement with previously published data for pyroxenes (e.g., Cloutis and Gaffey, 1991). On the other hand, Fe^{2+} crystal field band minima showed a negative dependence on the surface distribution parameter of active Fe^{2+} and consequently on the pyroxene modal abundance in norites, in contrast to what was expected (Fig. 3B). This is due to the inverse relationship between the abundance of spectrally active group in pyroxene (Fe^{2+}/M2 sites) and modal pyroxene in this suite of norites (Fig. 3C).

ROCK SPECTRAL CLASSIFICATION

The analysis and interpretation of rock spectral variability discussed in the previous section provide insights into characteristics and origin of the complex spectral properties of rocks. In order to manage this complexity properly and recognize it in remotely sensed data, appropriate methods of spectral classification within rock sets must be used.

Methodological Approaches for Rock Spectral Classification

Several methods for remote-sensing image spectra analysis and classification have been developed, based on various statistical and mathematical approaches. Two main approaches are generally followed: (1) classifying the unknown spectra by comparing them with either image-derived end members, or laboratory and field reference spectra (e.g., Mazer et al., 1988; Kruse et al., 1993); and (2) identifying and modeling absorption bands through: (a) absorption feature parameterization, with automatic detection of band positions, depths, and widths,

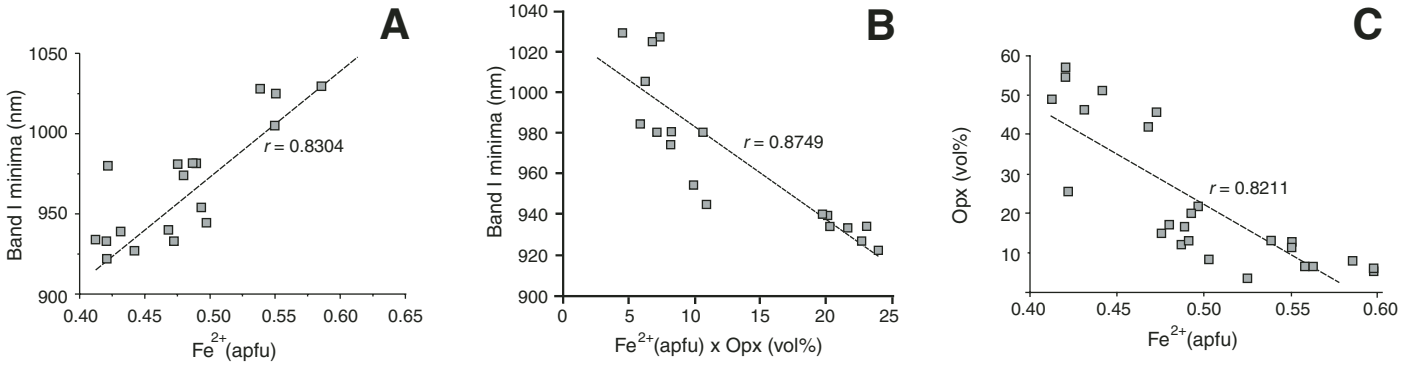

Figure 3. (A) Direct linear relationship between the divalent iron CF band minima and Fe^{2+}/M2 sites abundance (apfu) in pyroxene. (B) Inverse relationship between the iron CF band and Fe^{2+}/M2 sites abundance times modal orthopyroxene. (C) Inverse relationship between Fe^{2+}/M2 sites abundance and modal pyroxene. Data are from the suite of cumulates belonging to the Bjerkreim-Sokndal Layered Intrusion. See text for discussion.

after removal of the continuum (e.g., Clark and Roush, 1984; Kruse et al., 1988); (b) linear and nonlinear spectral mixing modeling, using either linear combinations of mineral spectra from reference libraries or theoretical calculations (e.g., Adams et al., 1986); and (c) curve-fitting by Gaussian and modified Gaussian distributions (Hawthorne and Waychunas, 1988; Sunshine et al., 1990, respectively), which provide the spectral decomposition in absorption bands actually related to absorption processes.

As the rocks are complex systems, classification criteria should combine the original Steno's facies concept, which refers to the external "appearance" of an object, with the appropriate genetic processes. In a rock spectrum, the basic "appearance" is represented by the absorption features, and the primary genetic processes are electronic transitions and vibrational motions within individual ions and cation-anion bonds (e.g., Hunt, 1980; Burns, 1993). As also discussed in the previous section, these processes are controlled by mineral chemistry and crystal structure and depend on physical and chemical conditions during rock formation, diagenesis, and weathering, according to the geologic context. Thus, a rock spectrum is the result of a complex chain of processes. To have an understanding of it, we need to both accurately disentangle the individual processes responsible for the spectral features, and infer the geologic significance involved in their association within the spectrum.

The empirical approach described here follows a number of steps. First, sets of absorption features occurring within the rock spectrum and attributable to absorption processes in individual minerals are isolated to form absorption patterns. Absorption patterns are thus related to mineral chemistry. Then the absorption patterns are combined into higher-order groups, which have been called spectrofacies (e.g., Fig. 4; Sgavetti et al., 1995; Ferrari et al., 1996). A spectrofacies represents an association of genetically related absorption patterns. It spectrally identifies a rock, i.e., a chemical system resulting from the physical-chemical conditions acting in a given geologic context at the time it formed. Within a spectrofacies, the spectral patterns are ranked according to the relative absorption intensities. The most prominent spectral patterns often represent the most abundant mineral in the rock. Occasionally, dominant patterns are due to modally subordinate phases, but again, they provide a description of the rock mineralogy, useful for the identification of rock types and geologic contexts.

Automatic or semiautomatic feature-finding algorithms included in software packages devoted to spectral analysis were used to identify and parameterize spectral bands (e.g., DISPEC, JPL, Grove et al., 1992; LABCALC®, Galactic Ind. Corp.; OriginLab® Corporation, www.originlab.com). These algorithms were able to identify band minima and calculate band parameters with the required accuracy.

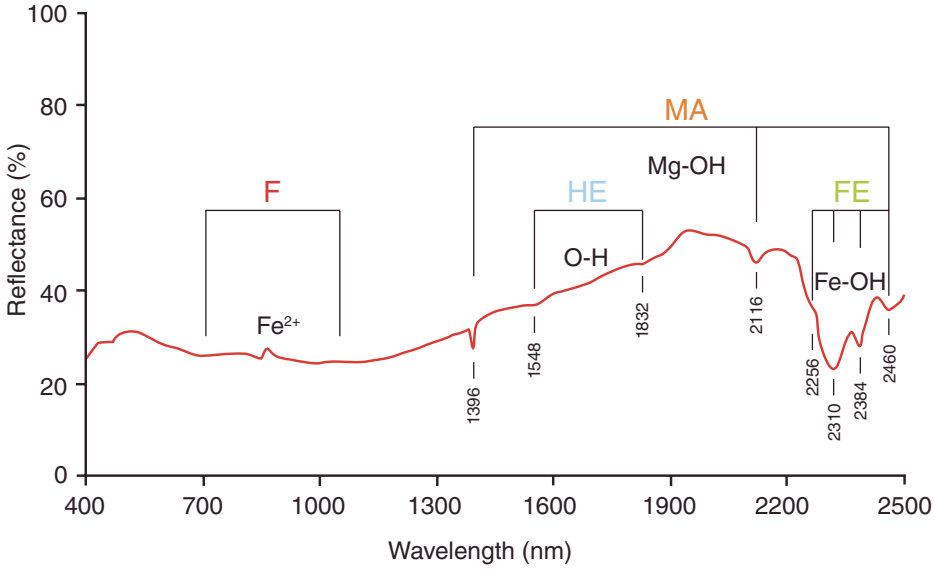

Figure 4. Example of spectral patterns and relative spectrofacies "MA HE FE F" in a bulk-rock spectrum (see Table 2 for symbol description). The spectrofacies is an association of spectral patterns; it spectrally characterizes the rock. The spectrum of this example was acquired on a gneiss from the metamorphic basement of central Madagascar.

Then, the empirical, concept-driven procedure based on identification of spectrofacies was followed.

The spectrofacies criterion proved to be particularly apt for classifying laboratory rock spectra dominated by groups of absorption features mainly due to vibrational processes, as shown below for muscovite-bearing metamorphic rocks. Further criteria are required for classifying rock spectra dominated by electronic absorptions, as for mafic igneous rocks. In particular, the spectral classification of mafic effusive rocks, with some effects due to texture and syneffusive alteration, needs to be improved.

Spectral Classification of Metamorphic and Mafic Volcanic Rocks

Laboratory spectra measured on rock slabs were used for the spectral classification of a suite of rocks belonging to pre-Paleozoic metamorphic sequences of the central Madagascar basement (Tables 2 and 3; Longhi et al., 2001) resulting in a tree-structure classification of spectrofacies. The first-order classes were based on dominant spectral patterns corresponding to the most abundant minerals or to the spectrally dominant species, and were represented by impure carbonate rocks, muscovite-bearing quartzites and micaschists, ferromagnesian rocks, and felsic rocks with abundant altered feldspar. Second-order classes, based on subordinate spectral patterns, described the spectral variability due to spectrally less active or less abundant phases. The spectral classes were used to interpret remotely acquired images of the area in which the rock samples were collected. Figure 5 is a spatial subset of TM images of central Madagascar. Band color composite 7, 4, 1 enhances a number of image units. Four of these units correspond to the first-order spectral classes listed in Table 3. They recur throughout the entire area investigated (not shown here), and the ground truth was provided by both the samples relative to the distinct units (Longhi et al., 2001) and existing lithologic maps (Moine, 1974). Higher-order classes, not discriminated in this image, are expected to be identified and mapped by hyperspectral sensors with proper spectral and spatial resolution and signal-to-noise ratio.

The spectral classification of basalts is relative to the Mount Etna (Italy) lava units ranging in age from 100 ka to the present (Romano, 1982). Spectral patterns, spectrofacies, and spectral classes were derived after the analysis of laboratory measurements on rock slab surfaces of lava samples (Tables 4 and 5). Figure 6 shows the representative spectra for each

TABLE 2. SPECTRAL PATTERNS IN METAMORPHIC ROCKS

Spectral pattern	Band position (nm)	Description
F	850/1200; 420/430; 480/500; 850/680	Fe^{2+}, Fe^{3+} electronic transitions in oxides and hydroxides minerals
L	680	π–π charge transfer in chlorophyll
CA	2334/2336; 1752/1760; 1880; 1990/1998; 2156/2160	CO_3^{2-} vibrational modes in calcite
CD	2316/2318; 1740; 1860	CO_3^{2-} vibrational modes in dolomite
CI	2316/2336	CO_3^{2-} vibrational modes in calcite-dolomite
HE	1540; 1828	OH^- vibrational modes in epidote
HF	1912; 1408; 2200; 2340; 2432	H_2O and OH^- vibrational modes in feldspar
HF_C	1912; 1408; 2200; 2340; 2432	H_2O and OH^- vibrational modes in Ca-rich feldspar
AM	2200; 1404; 2344; 2428; 2120; (1904)	Al-OH and OH^- vibrational modes in muscovite
AK	1392; 1408; 2160; 2200; 2308; 2372	OH^- and Al-OH vibrational modes in kaolinite
MA	2308; 2388; 1392; 2116; (2468)	Mg-OH vibrational modes in amphiboles
FE	2250	Fe-OH vibrational modes in epidote, biotite, tourmaline, chlorite, phlogopite
N		Flat spectrum

Note: Spectral patterns recognized within laboratory spectra of metamorphic rocks from the pre-Paleozoic basement of central Madagascar.

TABLE 3. SPECTRAL CLASSIFICATION OF METAMORPHIC ROCKS FROM THE CENTRAL MADAGASCAR CRYSTALLINE BASEMENT

First-order class: CA, CI — Impure marbles		First-order class: AM — Quartzites and micaschists	
Freshly cut surface	Weathered surface	Freshly cut surface	Weathered surface
$2\ CA_0$	$2\ CA_0$ (L)	$5\ AM_3$	$3\ AM_3$ (FE)
$3\ CA_1$ HF	$3\ CA_1$ HF	$5\ AM_3$	1 N (AM)
$3\ CA_2$	$3\ CA_2$	$5\ AM_2$ (FE)	$5\ AM_2$ FE (F)
$3\ CA_2$	$3\ CA_2$	$5\ AM_2$ (FE)	$4\ AM_2$ FE (F)
		$2\ AM_1$ (FE)	$3\ AM_2$ (FE)
		$3\ AM_1$ (FE)	$2\ AM_1$ FE (L)
$2\ CI_0$ (FE)	$2\ CI_0$ (FE)	$4\ AM_3$ FE	$3\ AM_3$ FE (L)
$2\ CI_2$ HF HF	$2\ CI_0$ (FE)	$3\ AM_2$ FE	$3\ AM_2$ FE (F)
$3\ CI_2$ FE HF	$2\ CI_2$ HF HF	$3\ AM_2$ FE	$3\ AM_2$ FE
$3\ CI_2$ FE HF F	$3\ CI_2$ FE HF	$2\ AM_1$ FE	$2\ AM_1$ FE
	$3\ CI_2$ FE HF F	$3\ AM_1$ FE	$2\ AM_1$ FE (L)
		$3\ AM_1$ FE	$1\ AM_0$
First-order class: HF — Quartz-rich gneisses and granofels		**First-order class: MA — Ferromagnesian rocks**	
Freshly cut surface	Weathered surface	Freshly cut surface	Weathered surface
$3\ HF_0$ FE	$3\ HF_1$		
$3\ HF_0$ FE	$2\ HF_0$ FE	$2\ MA_2$ FE	$2\ MA_1$ HF (F)
$2\ HF_0$ FE	$2\ HF_0$ FE F	$2\ MA_2$ FE (HF)	$2\ MA_2$ HF FE L
$2\ HF_0$ FE	$3\ HF_1$ FE	$2\ MA_1$ FE HF	$2\ MA_1$ FE HF
$3\ HF_2$ FE	$3\ HF_1$ FE		
$3\ HF_2$ FE (HE)	$3\ HF_1$ FE HE F	$1\ MA_2$ (HF)	$3\ HF_0$ (MA FE)
$5\ HF_2$ FE F	$5\ AK_2$ F	$2\ MA_2$ (HF FE)	$2\ MA_2$ (HF FE)
$3\ HF_1$ (FE) F	$3\ HF_0$ (FE) F	$2\ MA_2$ HF (FE)	$4\ AK_2$ (F)
$3\ HF_1$ (FE) F	$4\ HF_1$ F	$4\ MA_2$ HF FE HE	$4\ MA_2$ HF (FE) F
$4\ HF_0$ (MA FE)	$3\ HF_0$ (MA FE)	$3\ MA_2$ HE (FE)	$3\ MA_2$ FE (HF)
$3\ HF_1$ F	$3\ HF_0$ FE F		
$2\ FE_0$ HF	$2\ FE_0$ HF		
$2\ FE_0$ HF	$2\ FE_0$ HF		

Note: CA, CI, AM, HF, MA: dominant spectral patterns indicative of first-order classes. Horizontal lines separate second-order classes. Numbers 1–5 rank the overall spectral albedo. Albedo classes: 1: <16%; 2: 16%–25%; 3: 26%–35%; 4: 36%–45%; 5: >45%. Subscript numbers 0–3 rank increasing absorption intensities. Patterns in brackets are not always present. The rock suite includes carbonate and siliceous metamorphic rocks from the pre-Paleozoic basement of central Madagascar.

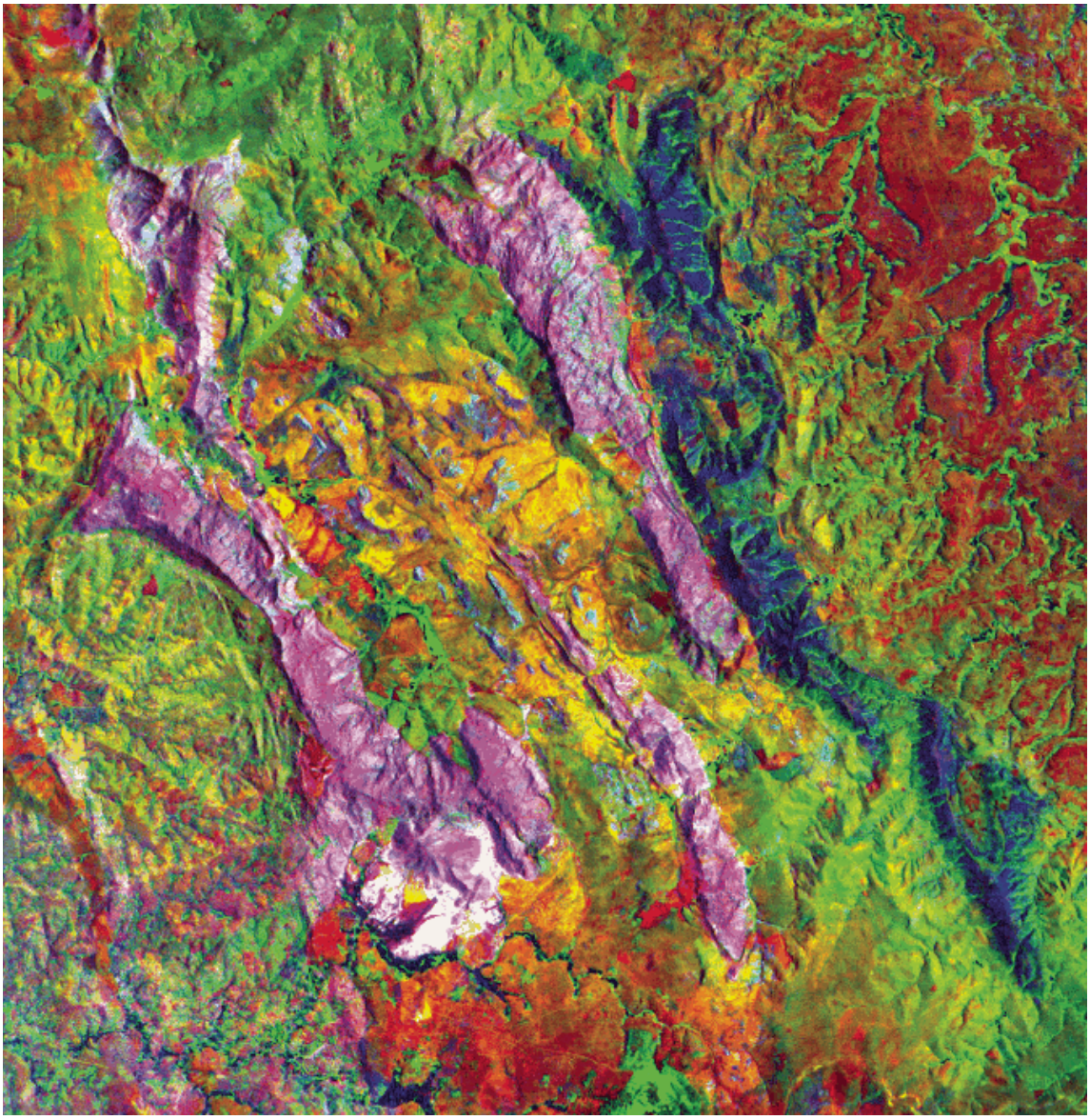

10 km

FIRST ORDER SPECTROFACIES

CA, CI marbles

AM quartzites and micaschists

HF quartz-rich gneisses and granofels

MA Fe-Mg rocks

OTHER SPECTRAL UNITS

Graphitic schists

Vegetation

Figure 5. Thematic Mapper (TM) image of a portion of the central Madagascar crystalline basement; color composite of 741 bands (2.215, 0.830, 0.485 μm). The color units in the image correlate with the first-order classes identified in the set of spectra measured on rock samples collected in the area and previous geologic map (Moine, 1974). CA, AM, HF, and MA—predominant spectral patterns (see Table 2), identifying first order classes (see Table 3).

TABLE 4. SPECTRAL PATTERNS IN BASALTIC ROCKS

Spectral pattern	Band position (nm)	Description
CT	<350	Charge transfer transitions in olivine; Ca-rich pyroxene and iron oxides
SFM	473–480	Spin-forbidden Fe^{2+} CF transitions in olivine and pyroxene
SFO	~450 510–570	Spin-forbidden Fe^{2+} and Fe^{3+} CF transitions strengthened by Fe^{3+}-Fe^{3+} magnetic coupling in iron oxides
CFH	~450 510–550 880–900	Fe^{2+} and Fe^{3+} CF transitions in hematite
CFM	1000–1100	Fe^{2+} CF transitions in olivine and Ca-rich pyroxene
WS	1050–1200	Broad band, probably due to overlapping absorptions of Fe-Mg silicates and plagioclase
WM	1800–2000	Broad band, probably due to overlapping absorptions of Fe-Mg silicates
VO	2200–2280	Metal-OH vibrational overtones due to hydration of Fe-Mg silicates
PS		Overall positive slope
NS		Overall negative slope

Note: The spectral patterns recognized in laboratory spectra of Mount Etna basalts. Slope characteristics are also indicated.

TABLE 5. SPECTRAL CLASSIFICATION OF MOUNT ETNA BASALTS

CFM							
	Representative sample	First-order class					
	E29	CT	SFM		CFM	VO	NS
	E11		SFM	SFO	CFM	VO	NS
WS							
	Representative sample	First-order class					
	E6			SFO	WS	VO	NS
	E25			[SFO]	WS	VO	NS
	E19				WS	VO	NS
PS							
	Representative sample	First-order class					
	PC5		SFM	SFO	[CFM]	VO	PS
WM							
	Representative sample	First-order class					
	E28		SFM	SFO	WM	VO	NS
	PC7	CT	SFM	CFH	WM	VO	NS

Note: First-order classes are based on features related to the overall spectral shape in the near-infrared (NIR) range. Different spectrofacies within first-order classes represent second-order classes. Square brackets indicate weak features.

class. The overall lava modal composition consists of plagioclase, clinopyroxene, olivine, and opaques, occurring as phenocrysts, embedded in a mostly microcrystalline and amorphous groundmass. In pyroclastic deposits, clinopyroxene is more abundant than plagioclase. Four first-order classes can be recognized on the basis of spectral patterns identified mainly according to the overall spectral shape. NIR absorption bands due to well-defined minerals (CFM spectral pattern in Table 4) are present in just one class of spectra. The very broad band centered in the NIR (WS and WM in Table 4), however, has a controversial interpretation. The slopes toward the infrared have positive or negative trends, probably depending on texture (Fig. 6). Second-order classes are based on several weak absorption bands due to electronic transitions in Fe-bearing minerals in the VIS region. Only the representative spectrofacies for each second-order class are reported in Table 5. The combined effect of texture, type, and degree of alteration, neutral dark components, and amorphous groundmass is still not fully understood. The basalt spectra are discussed in more detail in the following section.

INTEGRATING MULTISCALE DATA: PRELIMINARY RESULTS OF A SURVEY OF RECENT LAVA FLOWS ON MOUNT ETNA

Hyperion and ASTER satellite images of Mount Etna volcano were acquired in July 2003 (Buongiorno et al., 2006), after the intense activity at the end of 2002 and in the first months of 2003. During this eruptive phase, a number of lava flows were emplaced on both the northeast and south flanks of the volcano (Fig. 7). Contemporaneous remote-sensing and in situ measurements (Table 6) and sampling of different rock units were carried out.

Mount Etna is a middle Pleistocene to present volcanic complex. Lava composition has slightly changed through time, from intermediate to sodic, progressively high-K rock kindred, toward alkali-basalt and hawaiites (e.g., Romano, 1982; Cristofolini et al., 1987; Armienti et al., 1994).

Five main types of surface characterize the volcanic complex (Fig. 8). The most ancient lava flows are covered by thick and fresh vegetation, and hence they are not included in this discussion. The surface types considered here include: (1) historic lava flows (1600–1900 A.D.), covered by scattered bushes, lichens, and coatings of iron oxides and weathering-derived products (Fig. 8A); (2) pyroclastic deposits (tephra) consisting of ash and small-sized (centimetric) scoriae (Fig. 8B), which drape wide and flat regions within the huge ancient caldera near the top of the complex, the flanks of main craters, and the southern and eastern flanks of the volcano (Andronico et al., 2005); (3) the most recent lava flows (emplaced during 2001–2003 eruptions), characterized by piled, very coarse scoriae and ash (Fig. 8C); and (4) portions of recent lava flows consisting of reddish scoriae produced by syneffusive oxidation, which is extremely intense near the effusive centers (Fig. 8D). Factors such as ash concentration, size and shape of the scoriae, alteration, degree of weathering, and lichen coating all control the surface texture and roughness on various scales. Texture radiometric effects are expected to be superimposed on the spectral features of fresh and altered lavas.

Integrating Field and Satellite Hyperspectral Data: Image Data Classification

In situ measurements were made on lava flows emplaced during the 1792 and 2001–2003 eruptions, both on distal and proximal positions with respect to the effusive centers. Various pyroclastic deposits were also

measured on the south and northeast flanks of the volcano (Table 6).

Four classes of field spectra were identified and are shown in Figure 8. Spectra of pyroclastic deposits ("pyroclastics") and slightly oxidized lava ("lava") (Figs. 8B and 8C) are comparable to each other in terms of overall reflectance and position of the reflectance peak. The main differences regard the slope toward long wavelengths and the position of minima of the very broad absorption in the near-infrared interval. Spectra of strongly oxidized lava, measured in the proximal portions of the most recent lava flows (Fig. 8D), are dominated by the signature of hematite, although features due to other components can also be recognized, as discussed in the following section. Spectra of historic lava ("altered lava" in Fig. 8A) show a shoulder at wavelengths longer than the reflectance maxima of previous spectral classes, and a flat or slightly convex profile in the 0.75 and 2.5 µm wavelength range. A weak absorption feature near 0.5 µm always occurs in all the spectral classes.

Hyperion data have 10 nm nominal spectral resolution and 30 m ground resolution, and are therefore more powerful than ASTER data for mineralogical mapping in the VIS-NIR range (Table 1). Hyperion images used in this paper were corrected for atmospheric effects and calibrated to reflectance (Buongiorno et al., 2006). A Hyperion color-composite image of the northeast sector of the volcano is shown in Figure 9A. Hyperion data still proved to be affected by nonremovable noise, as shown in Figures 10B–D and 11B–E. For this reason, the Spectral Angle Mapper (SAM) provided with the ENVI® software package appeared to be the most suitable classification method. SAM classification treats pixel and end-member spectra as vectors in a space with dimensionality equal to the number of bands, and determines the similarity between individual pixels and end-member spectra by calculating the angle between the vectors (e.g., Kruse et al., 1993). The end members for the classification of Mount Etna Hyperion image are represented by in situ measurements and linear combinations resulting from them (Figs. 9C). Class statistics are reported in Table 7. SAM accuracy is in general evaluated through confusion matrix analysis, by comparing the classification results with a ground-truth image or pixels from the image. However, the purposes of this paper, i.e., comparison of data acquired in different experimental settings, required a different evaluation approach, and SAM accuracy was evaluated by directly comparing classified data with the end-member field spectra used for the classification (Figs. 10 and 11; Table 8).

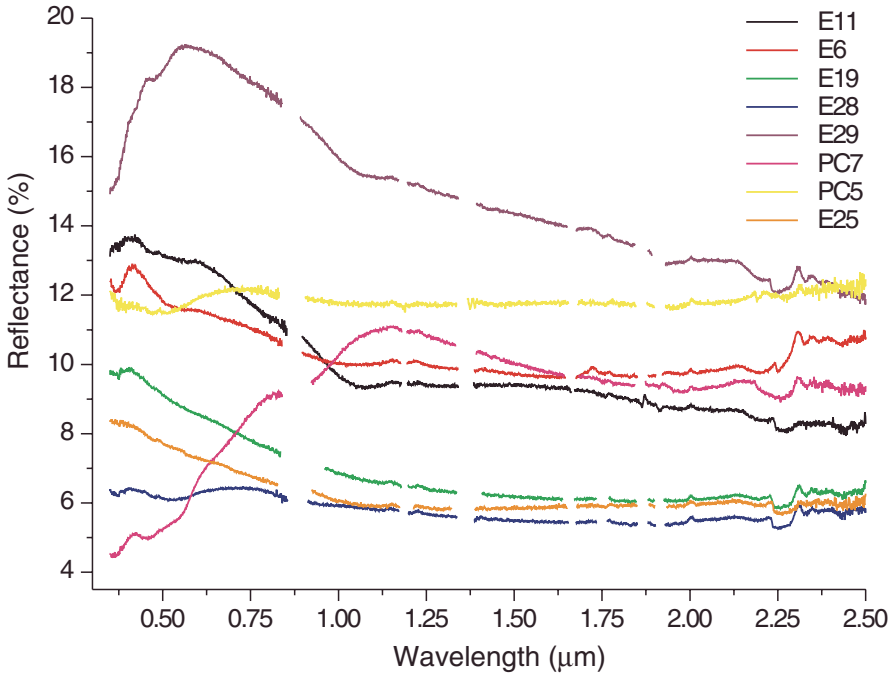

Figure 6. Laboratory reflectance spectra of Mount Etna basalts, representative of the spectral classes shown in Table 5. E29: ancient lava (~100 ka); E6, E19: historic lava (1766 and 1970 flows, respectively); E11 and E25: 2002–2003 distal lava flow, south and northeast Mount Etna flanks, respectively; PC7 and E28: 2002–2003 proximal and intermediate lavas, respectively, northeast Mount Etna flank; PC5: pyroclastic deposits, northeast Mount Etna flank.

Materials with the composition of slightly oxidized lavas (lava) constitute most of the area (Fig. 9B). Materials represented by tephra spectrum (pyroclastics) concentrate around the major effusive centers and along the northeast fracture. Very recent lava flows (see detail in Fig. 10A) are classified as "lava" and "pyroclastics" along their axial zone, while their borders include a number of pixels classified as "pyroclastics/lava/oxidized" and as "altered" because of the presence of iron oxides and weathering products. The average spectra of three image classes are shown in Figures 10B–10D, where they are compared with the corresponding end members. The standard deviation for each class of spectra and the root mean square (RMS) error between class average spectra and relative end members are listed in Table 8. A quite good spectral correlation can be observed (RMS ≤ 0.005).

Volcanic products affected by different degrees of alteration are concentrically distributed around recent effusive centers. Figure 11A shows that this distribution is apparently also controlled by the downdip flow direction of the effusive products along the northeast slope of Mount Etna. Transitions from materials containing both iron oxides (oxidized) and weathering products (altered/lava, altered, and lava/oxidized), to mixtures of variously altered lava (lava, lava/oxidized) have been identified moving from the center outward. Except for the "lava/oxidized" class, for most of these materials, the correlation between average spectra of individual SAM classes and relative end members was poorer than for recent lava and tephra. In this case, average class spectra best compare with linear combinations of end-member field spectra not coinciding exactly with the end-member combinations used for the classification (Fig. 11B–E; Table 8).

Comparison Between Laboratory and Field Data

The comparison between laboratory and in situ measurements discussed in detail here regards recent lava (E25 in Fig. 6 and "lava" in Fig. 8C), tephra (PC5 in Fig. 6 and "pyroclastics" in Fig. 8B), and proximal oxidized lava (PC7 in Fig. 6 and "oxidized lava" in Fig. 8D). Laboratory spectra of historic lava (E19 in Fig. 6) are very similar to those of recent lava, whereas the corresponding in situ spectra (Fig. 8) are not comparable to each other. This is intrinsic to the laboratory operational method for accomplishing measurements on exposed, altered surfaces. According to alteration rim thickness and surface roughness, the alteration coating can be destroyed

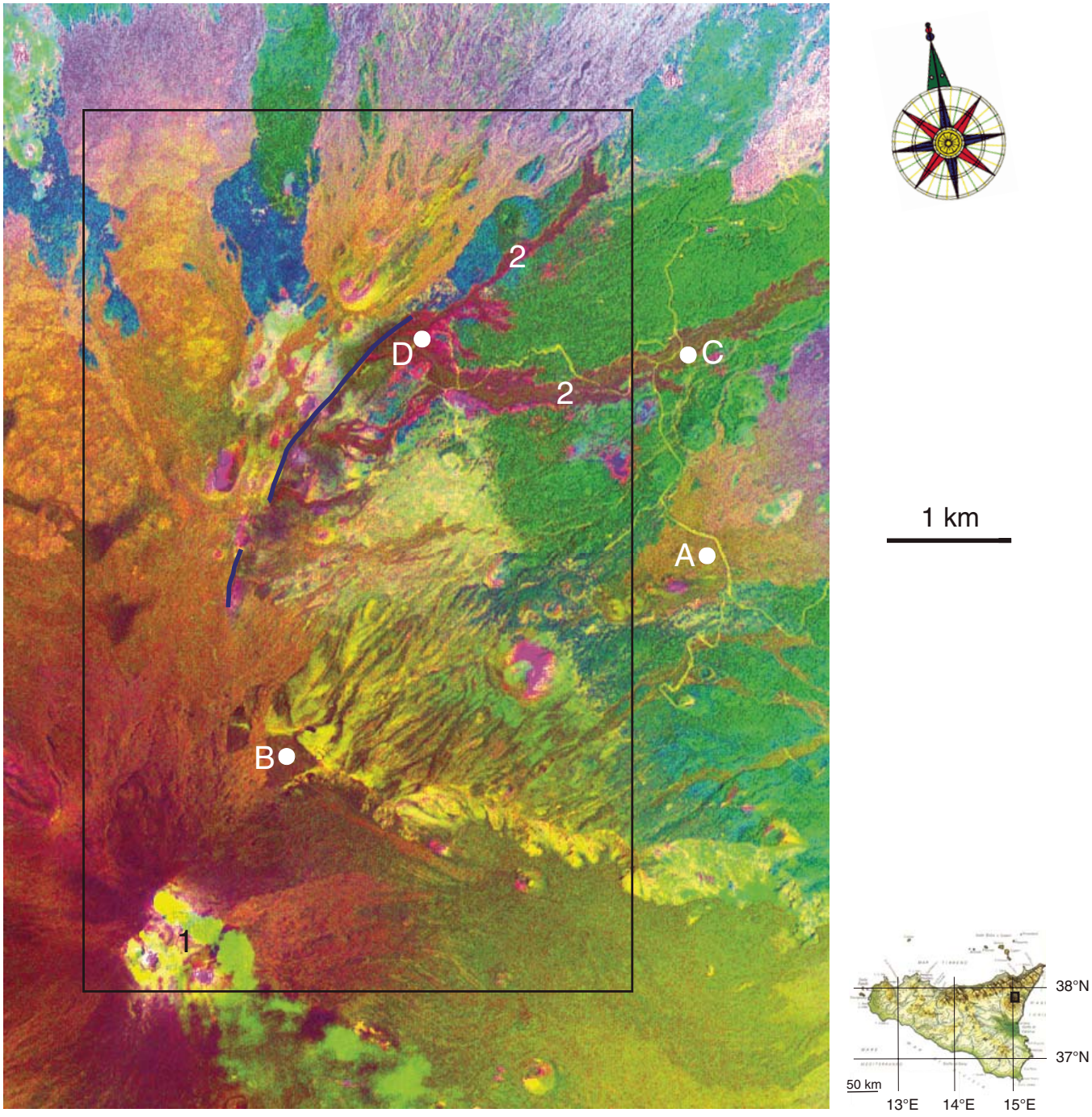

Figure 7. Advanced spaceborne thermal emission and reflection radiometer (ASTER) image of the northeast portion of Mount Etna, acquired on 19 July 2003; RGB (red-green-blue) color composite of 217 bands (0.660, 0.560, 2260 µm) with decorrelation stretching. 1: summit cone complex; 2: 2002–2003 lava flows; A, B, C, D: location of the field sites of Figure 8; thick black line: location of the 2002 fracture, source of the recent flows; box: location of Figure 9A–B.

TABLE 6. IN SITU REFLECTANCE MEASUREMENTS ON MOUNT ETNA

Date	Site	Location		Number of spectra	Geologic unit	Elevation (m a.s.l.)	GMT time	Contemporaneous
		Lat. (°N)	Long. (°E)					
17/07/2003	South flank, W Monti Silvestri	37°42'02.5"	15°00'11.4"	15	2001 lava flow clean and altered	1950	11:00–11:40	Rock sampling
17/07/2003	South flank, Rifugio Sapienza	37°41'57.8"	15°00'00.2"	6	2002–2003 lava flow clean and altered	1894	13:00	Rock sampling
19/07/2003	NE flank, Piano delle Concazze	37°46'00.0"	15°00'43.4"	97	Ash and scoriae	2793	10:30–11:30	Rock sampling; ASTER and Hyperion overflight
23/07/2003	NE flank, Piano delle Concazze	37°45'58.0"	15°00'39.6"	12	Buried snow	2796	11:40–12:00	Rock sampling
22/07/2003	NE flank, Strada per Linguaglossa	37°47'41.9"	15°03' 41.9"	18	2002–2003 lava flow clean and altered	1516	8:00–11:00	Rock sampling
23/07/2003	NE flank, Piano Provenzana	37°48'11.2"	15°02'10.4"	18	2002–2003 lava flow clean and altered	1858	8:15–10:15	Rock sampling
21/07/2003	ENE flank, Statale SP 92, km 32	37°41'37.0"	15°04'57.5"	54	1792 lava flow clean and altered	1014	9:00	Rock sampling

Note: Measurements on historic and recent lava flow units with different degrees of alteration. See text for details on data acquisition procedures. Cloud cover absent.

during rock slab preparation for laboratory measurements. The spectral features observed in laboratory reflectance spectra are interpreted through petrographic analyses.

In the NIR region, both laboratory and in situ measurements of recent lava are characterized by a slightly negative slope and a shallow concavity at wavelengths longer than 0.7 µm (Fig. 12A). We attribute this broad band to the superposition of a number of crystal field transitions in Fe^{2+} in mostly zoned Ca-rich pyroxene, olivine, and plagioclase (cf. "[SFO] WS VO NS" spectrofacies in Table 5 and spectrum E25 in Fig. 6). Alternatively, it can be interpreted as the effect of the porphyritic texture of basalt, which is responsible for the coexistence of phenocrysts embedded in a poorly crystalline, mostly glassy groundmass. Note that laboratory spectra broad-band minima are shifted toward shorter wavelengths with respect to the in situ spectrum (Fig. 12A).

In the same NIR region, the laboratory spectrum of tephra samples (Fig. 12B) has an overall flatter profile than in situ measurements, in which an absorption due to ferromagnesian minerals can possibly be recognized (SFM SFO [CFM] VO PS spectrofacies in Table 5 and PC5 in Fig. 6). In contrast, the in situ spectrum shows a broad band similar to that observed in recent lava spectra (WS spectral pattern in Table 4). Tephra spectra are characterized by a slightly positive slope, likely due to the particulate nature of this material.

In the VIS interval, laboratory spectra of recent lava slab surfaces show generally weak absorption bands at 0.473, 0.513, 0.572 µm (Fig. 12C; SFO pattern in Table 4; cf. E25 and E11 spectra in Fig. 6). These band minima can be attributed to spin-forbidden crystal field transitions in a number of cations occurring as trace elements within olivine and Ca-rich pyroxene, both fresh and oxidized (King and Ridley, 1987; Straub et al., 1991; Cloutis, 2002). In situ measurements of recent lava display a single absorption in this region, at 0.47 µm. However, the most significant difference between the two types of spectra is the opposite slope shape toward the UV, shown in Figure 12A.

In the same VIS range, a tephra laboratory spectrum shows two absorption bands at 0.40 and 0.52 µm (Fig. 12D), both assigned to spin-forbidden transitions in iron oxides (patterns SFO in Table 4). In the field spectrum, the two bands are shifted to 0.48 and 0.54 µm, respectively.

The several discrepancies observed in the laboratory and field VIS-NIR spectra of recent lava and tephra are further discussed in the following section, although they are the object of in progress studies.

The absorption features occurring within the vibrational overtone region are diagnostic of weathering products, also observed in the field.

Field and laboratory spectra of highly oxidized lava, measured in proximity to the effusive centers, are significantly similar to each other for both band positions and intensities (Fig. 13; CT CFH WM VO NS spectrofacies in Table 5 and PC7 in Figure 6; "oxidized lava" in Fig. 8D). They are characterized by a reflectance peak at 1.20–1.25 µm and three weak bands near 0.50 and at 0.90 µm superimposed on the strong charge transfer band in the UV (Figs. 13A, 13C, and 13D), and represent a spectral pattern diagnostic of hematite (cf. Fig. 13B). The near-infrared composite absorption feature in both spectra, although shifted to 1.6–2.0 µm, is still consistent with the presence of pyroxene (WM pattern in Table 4). A secondary absorption peak at 2.2 µm still relates to alteration products (VO pattern).

DISCUSSION

Two major problems arise from the analysis of the three data sets. The first is the noise level in the remote data, which required several sensor channels to remove, mostly in the short wavelength region. As a consequence, the observation of some of the iron absorption bands critical for main composition and alteration analyses was precluded. Nevertheless, a certain similarity was observed between remotely sensed and field data, and, actually, field spectra proved to be suitable end members for the classification of the remotely acquired spectra of Mount Etna basalts and pyroclastic deposits. A lower accuracy was obtained in the classification of variously altered and oxidized materials, likely consisting of intimately mixed minerals. They were probably not systematically measured in the field, emphasizing the importance of appropriate end members for any image data classification procedure.

The second problem is the peculiar shape of the laboratory basalt spectra, particularly in the VIS and toward the UV, which is in contrast to the field spectra of the same rocks. As a result, only two of the spectral classes determined through laboratory spectroscopy (represented by spectra PC5 and PC7 in Fig. 6) clearly correspond to field spectral classes ("pyroclastic" and "oxidized lava," respectively in Figs. 8C and 8D). The CFM class of laboratory spectra in Table 5 also includes the ancient lava (E29 in Fig. 6), for which field spectroscopy is not available. The ancient lava spectrum shows charge transfer absorption bands in the UV (CT pattern in Table 4), which produce a peak of reflectance in the VIS. The pronounced negative slope at longer wavelengths is quite common in mafic rock spectra (Harloff and Arnold, 2001;

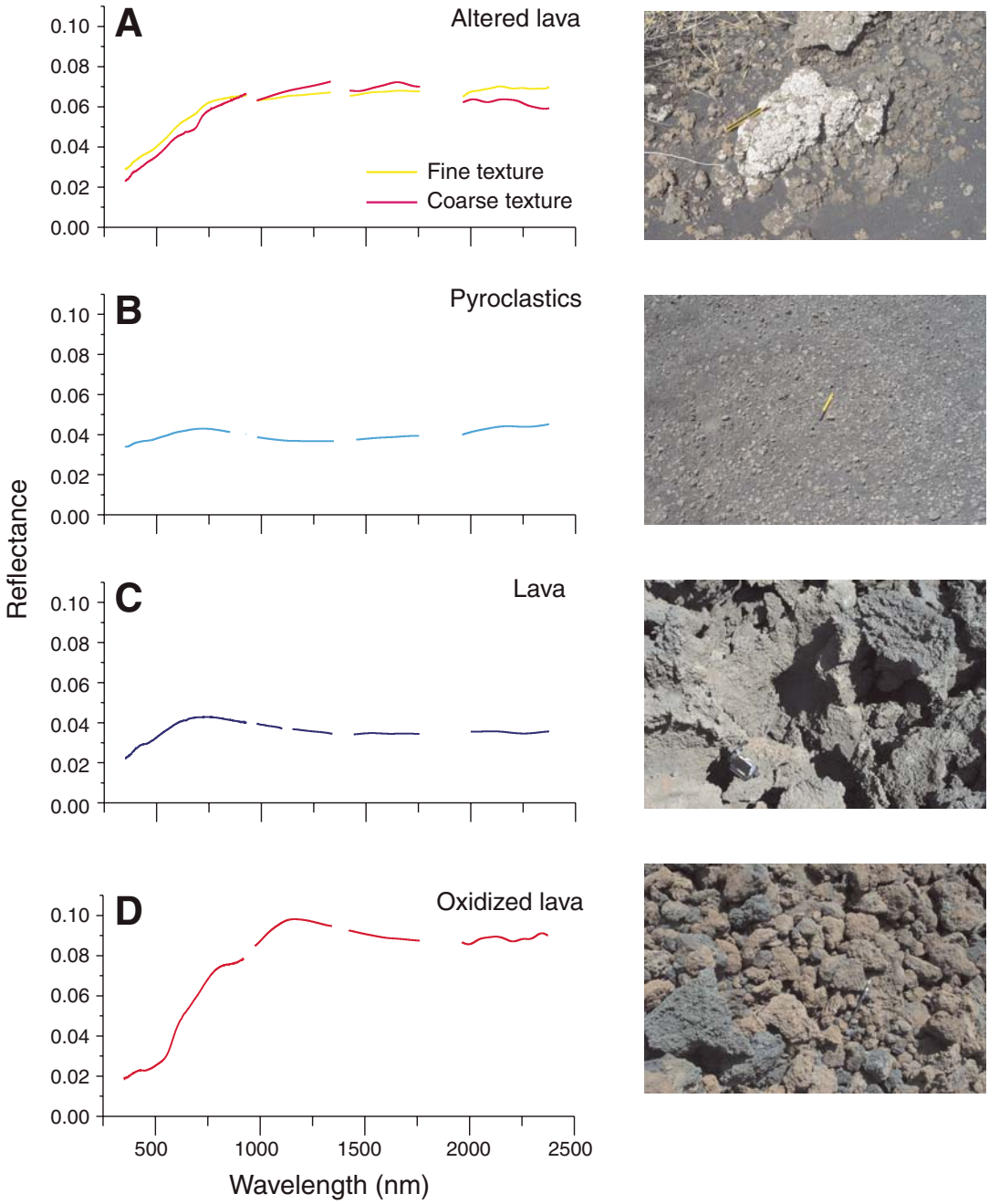

Figure 8. Reflectance spectra measured in the field using an ASD FieldSpec Pro FR (left side), and pictures of the measured surfaces (right side). Locations are in Figure 7. Missing values in the spectra correspond to detector change and atmospheric water bands. The spectra were smoothed using Fourier transform methods using 20 points as algorithm input. The spectra are representative of four characteristic surfaces: (A) "altered lava": lava with iron oxides and clay minerals alteration, both coarse and fine surface textures; (B) "pyroclastics": pyroclastic deposits consisting of ash and centimetric scoriae; (C) "lava": slightly altered, blocky recent lava; (D) "oxidized lava": lava with predominant iron-oxide alteration, mainly occurring very close to the effusive centers. See text for explanations.

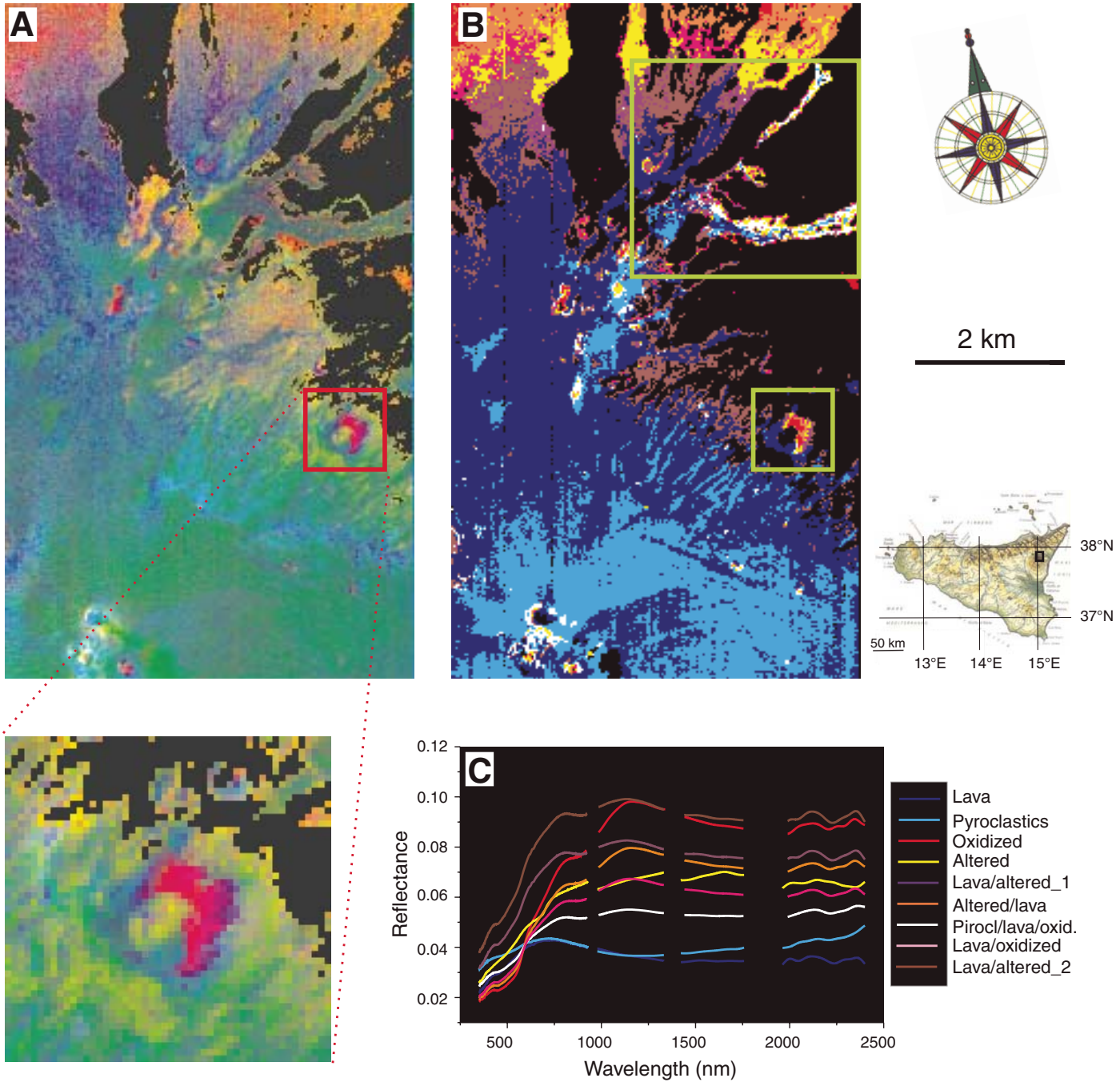

Figure 9. (A) Hyperion image of the northeast portion of Mount Etna, acquired on 19 July 2003; see location in Figure 7; RGB (red-green-blue) color composite of 122 11 21 bands (1.750, 0.538, 0.630 µm), with decorrelation stretching; vegetation is masked. Inset: detail of a lateral cone. (B) Spectral Angle Mapper (SAM) classification of the same area as in A, with 0.18 rad spectral angle. (C) End-member spectra used for the SAM classification: "pyroclastics," "lava," and "oxidized" correspond to the spectra of Figure 8B–D, respectively; "altered": average of Figure 8A spectra; "lava/altered_1" and "lava/altered_2": linear combinations of predominant "lava" and subordinate "altered lava" spectra, with different albedos; "altered/lava": linear combination of predominant "altered lava" and subordinate " lava" spectra; "pyrocl/lava/oxid": linear combination of "pyroclastics," "lava," and "oxidized lava" spectra, in almost equal proportions; "lava/oxidized": linear combination of "lava" and "oxidized lava" in equal proportions. Large and small boxes in B are locations of Figures 10A and 11A, respectively.

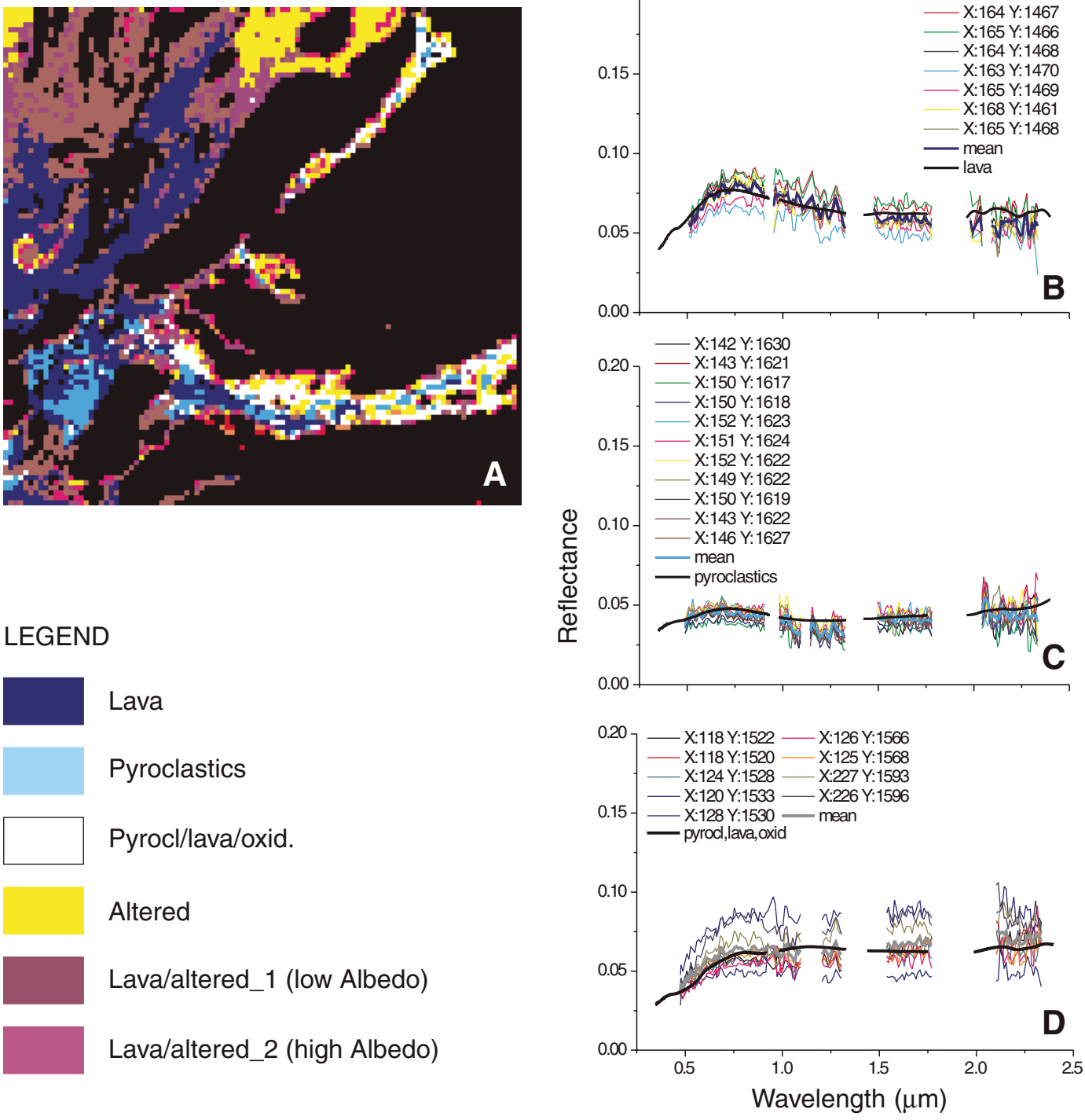

Figure 10. (A) Detail of Figure 9B (large box) showing the 2002–2003 lava flows. (B–D) Spectral profiles (thin lines) of pixels from Spectral Angle Mapper (SAM) classes, average spectral profile (thick color line), and field end member (thick black line). Pixel spectral profiles were classified with angles ≤0.1 rad. The classes are: (B) lava, (C) pyroclastics, (D) pyrocl/lava/oxidized. See Figure 9C for end-member descriptions and Table 8 for the accuracy of spectral matches.

Pompilio, 2005a). When considering the spectral classes represented by other spectra, such as E11, E6, E25, E19, the most impressive discrepancies with both the ancient lava and in situ spectra regard the absence of the CT pattern. These laboratory spectra are relative to basalts from both distal areas of recent flows, and historic lava flows.

In spite of the quite similar mineral and chemical composition, both differences and similarities in basalt laboratory spectra did not appear to correlate to variations in the petrographic parameters determined by standard analysis, such as the porphyritic and vesiculation indexes. One hypothesis could be that, for these extremely low-reflectance rocks, the spectroscopic effects of high amounts of opaque and amorphous phases are exceedingly relevant (Hapke, 2001), particularly if these phases are a significant constituent of the micro- and submicrocrystalline groundmass. Particularly complex interactions between compositional and geometric parameters, such as grain size, crystallinity, viewing geometry, and texture, can also be expected. Answering the questions raised by the set of rocks discussed here is of primary importance to bridge the gap between laboratory and both field and remotely acquired data, and is critical to obtain a geologically significant output from hyperspectral data analysis and classification.

Nevertheless, in situ spectra were interpreted using spectral patterns and spectrofacies identified in laboratory spectra, and some of the end members for remote data classification were selected starting from in situ spectra closely corresponding to spectral classes determined through laboratory spectral classification. The conceptual background for this procedure was that spectral patterns and spectrofacies identified in laboratory spectra provide synthetic descriptions of interaction processes in minerals and whole-rock spectral properties that can be identified also in data at different scales. The concept of spectral classifications described in this paper was primarily developed for outcropping rocks with negligible or limited surface weathering, i.e., under conditions that are unable to significantly mask the clean rock absorption features. In the case of intense surface weathering, spectra of exposed rock surfaces must be included in the classification, with consequent addition of new spectral patterns.

Within individual spectrofacies, some rock spectral features can systematically or nonsystematically vary in wavelength position or intensity. The systematic shift of specific absorption band minima is expected to be somewhat correlated with well-defined mineral chemistry variations, which in turn are related to the geologic processes responsible for the rock formation. The analysis of rock spectral variability therefore provides the geologic conceptual background for the interpretation of spectroscopic data at every scale. In the examples discussed in this paper, the wavelength shift of the diagnostic absorption bands was found to be either directly or inversely dependent on the abundance of spectroscopically active groups within the minerals. The geologic processes, either the fractional crystallization from a melt or the rock transformation by metamorphism, evolved according to those relationships. However, in rocks with a high content of minerals that can be spectrally active, the relationships between position of the absorption band minima and mineral abundance can be lacking or even reversed with respect to the band position versus spectrally active group relationship. This depends on the degree and type of the correlation existing between mineral and bulk chemistry, constrained by the evolutionary history of the geologic system. Therefore, the systematic analysis of the relationship between bulk-rock composition and spectrally active group should always be considered in bulk-rock spectral modeling.

When sets of multiscale spectroscopic data are not available for an area, the concept of spectrofacies can be used to classify mineral and bulk-rock spectra from available spectral libraries. This classification can be assisted by existing calibration curves and by improved understanding of the other factors affecting the bulk-rock spectra, such as texture and crystallinity. This can also provide the geologic rationale for the use of expert systems that run multifeature identification algorithms and decision-making processes (e.g., Clark et al., 2003), thus optimizing the lithologic analysis of remote-sensing data.

TABLE 7. STATISTICS FOR SPECTRAL ANGLE MAPPER–DERIVED CLASSES

Classes	No. pixels	%	Angle values			
			Min.	Max.	Mean	S.d.
Unclassified	8667	17.55				
Lava	20,321	41.15	0.059	0.180	0.121	0.021
Pyroclastics	10,058	20.37	0.057	0.180	0.122	0.017
Oxidized	322	0.65	0.062	0.179	0.119	0.019
Altered	1733	3.51	0.049	0.178	0.095	0.017
Lava/altered_1	1099	2.23	0.058	0.179	0.107	0.019
Altered/lava	1816	3.68	0.052	0.180	0.109	0.021
Pyrocl/lava/oxid.	806	1.63	0.054	0.176	0.115	0.026
Lava/oxidized	983	1.99	0.059	0.180	0.119	0.030
Lava/altered_2	3583	7.25	0.063	0.180	0.134	0.025
Total for classification	49,388	100.00				
Mask	9580					
Total	58,968					
Accuracy		0.825				

Note: Classification angle: 0.18 rad = ~10°. Masked pixels were not computed in the statistics.
S.d.—standard deviation.

CONCLUDING REMARKS

Spectroscopy at various scales has a direct application in remote data interpretation. A remote-sensing survey is an intrinsically multiscale survey, both when in situ measurements and sampling return for laboratory spectroscopy are performed concomitantly with the air/spaceborne sensor overpass, and in frontier exploration surveys, where, in the absence of ground data from the study area, remotely acquired spectra have to be interpreted through comparison with pre-existing laboratory

TABLE 8. SPECTRAL ANGLE MAPPER (SAM) SPECTRAL ACCURACY

Classes	S.d.	RMS
Lava	0.007	0.004*
Pyroclastics	0.042	0.004†
Oxidized	0.008	0.023§
Altered	0.017	0.01#
Lava/altered_1	0.021	0.008**
Altered/lava	0.015	0.01††
Pyrocl/lava/oxid.	0.012	0.004§§
Lava/oxidized	0.018	0.005##
Lava/altered_2	0.012	0.007***

Note: S.d. indicates the standard deviations of average pixel spectra compared to SAM-derived pixel spectra selected according to angles up to 0.1 rad. RMS indicates the root mean square error between average pixel spectra from SAM classes and linear combinations of field spectra:
*, †, §§, ## RMS with end members used for SAM;
§, **, †† RMS with other spectral mixings. In particular:
§ "oxidized lava" and "altered lava" in almost equal abundance;
** predominant "lava" and subordinate "altered lava";
†† "oxidized lava," "altered lava," and "lava" in order of abundance.
# and *** not shown here.

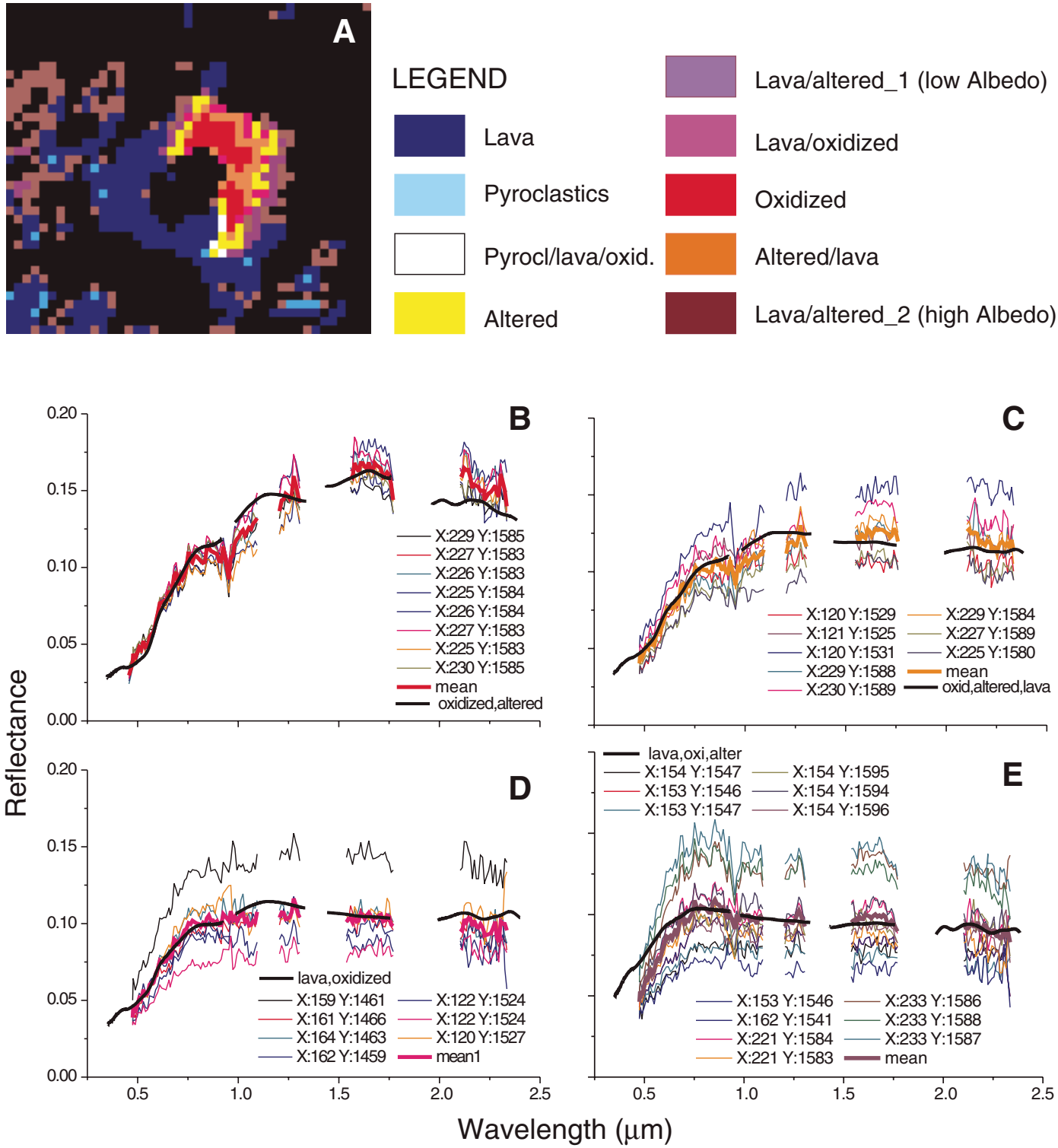

Figure 11. (A) Detail of Figure 9B (small box) showing the Spectral Angle Mapper (SAM) classification of a minor, lateral cone. Variously altered volcanic materials form concentric aprons around the crater on the downdip slope with respect to the Mount Etna northeast flank, downwind of the plume. (B–E) Spectral profiles (thin lines) of pixels from SAM classes, average spectral profile (thick color lines), and field spectrum (thick black lines). Pixel spectral profiles classified with angles ≤0.1 rad. SAM classes are: (B) oxidized, (C) altered/lava, (D) lava/oxidized, (E) lava/altered_1. See Figure 9C for end-member descriptions. Except for the "lava/oxidized" class (D), average spectra of the other classes best compare with field spectra linear combinations not coinciding exactly with those of the relative class end members. Mixed spectra reported here are: (B) oxidized lava and altered lava in almost equal proportions; (C) oxidized lava, altered lava, and lava in order of decreasing proportions; (E) predominant lava and subordinate oxidized lava and altered lava. See Table 8 for the accuracy of spectral matches.

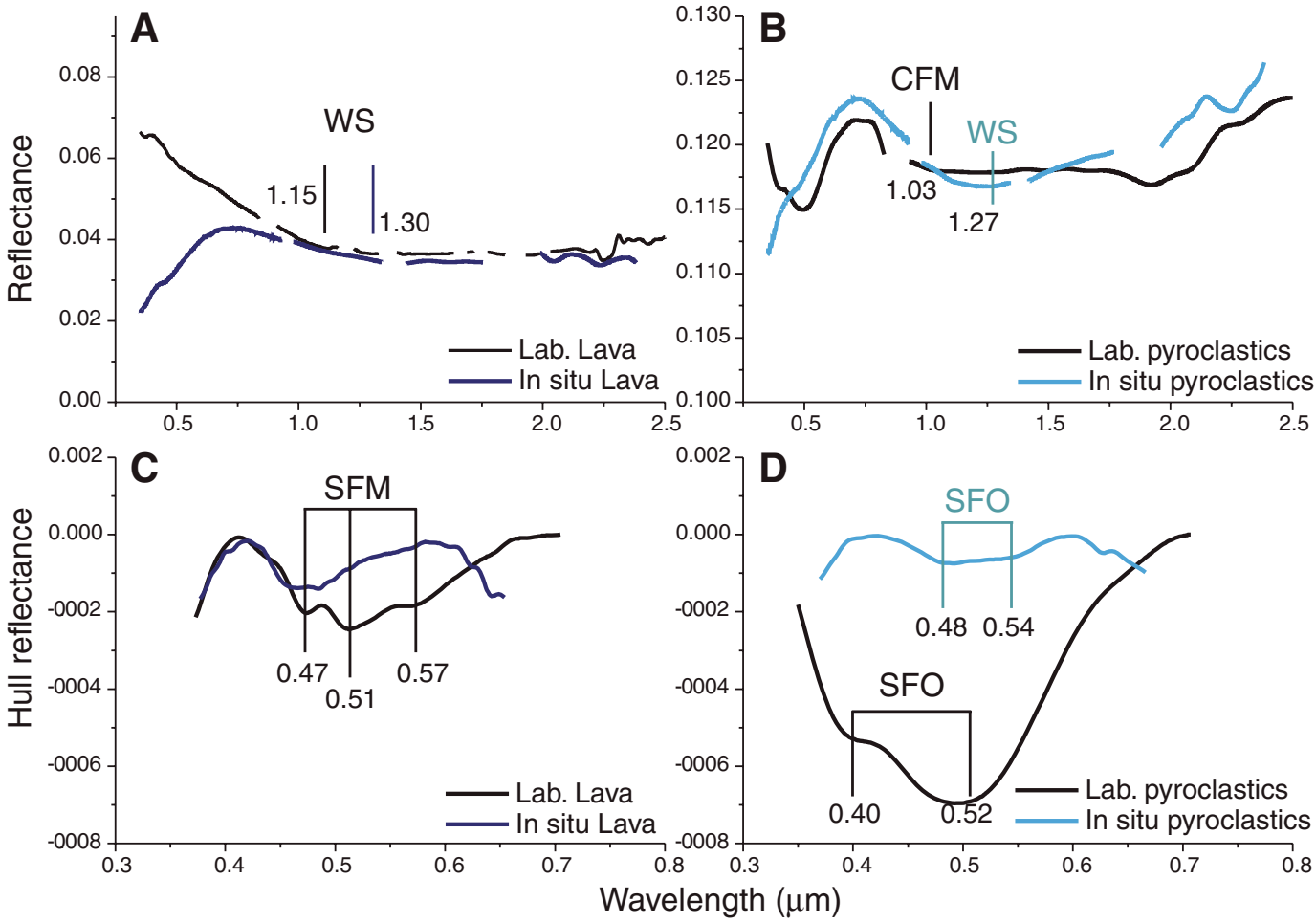

Figure 12. Comparison between laboratory and field spectra. (A) Slightly oxidized distal lava; and (B) pyroclastic deposits. Lava spectrum is 15% offset for a better comparison. (C) and (D): Continuum-removed spectra of the VIS (visible) range of A and B, respectively. The absorption intensity is variable. WS, CFM, SFM, and SFO indicate the spectral patterns (see Table 4 for explanation). See discussion in text.

spectral libraries. In both cases, understanding the remotely acquired spectra strongly depends on the accuracy of the relationships between spectroscopic features and rock chemical and mineralogical composition. Integrated spectroscopic and petrographic-mineralogical laboratory measurements are the primary tool to set up the scientific background for spectral features assignment, identify calibration curves, and also develop classification criteria, that, with proper scaling, can be applied to the different experimental conditions.

Spectroscopic calibration curves involving spectroscopically active groups can be established in sets of pure minerals and bulk-rock suites: two examples illustrated this issue relative to metamorphic rocks and cumulates. In both cases, the important role of the bulk-rock composition in controlling the parameters of the calibration curves and their applicability to quantitative determinations has been demonstrated. Understanding bulk-rock effects is critical, because the rock spectral variabilities record the rock-forming geologic processes, and therefore provide the geologic conceptual background for spectroscopic data interpretation.

Selection of end members for image data classification should include the concept of spectrofacies, i.e., a synthetic representation of rock spectral characteristics. We reported two examples of rock classification based on laboratory spectra, relative to metamorphic rocks and basalts. Different orders of classes were identified, potentially recognizable in remotely acquired images, according to the sensor resolution.

In the Mount Etna multiscale survey, individual field spectra and linear combinations of field spectra represented suitable end members for satellite hyperspectral data classification, except for the case of probable intimate mixtures of minerals. On the other hand, only a limited number of basalt spectral classes determined by laboratory spectroscopy were comparable to field spectral classes. The usefulness of laboratory spectra was, in this case, more related to absorption features assignment than as end members for image classification.

Basalts are rocks for which the relationship between spectral characteristics and compositional variation has not yet been systematically analyzed. Work in progress includes extended analyses of groundmass composition, crystallinity degree, vesiculation patterns and relationship with alteration, relative roles of phenocrysts, microphenocrysts, submicroscopic and amorphous phases, and the nature of alteration processes. As basalts are important constituents of Earth's surface and are inferred to be the primary components of other bodies of the solar system, understanding the spectral properties of these rocks on different scales is critical for building spectral libraries appropriate to the analysis of those surfaces.

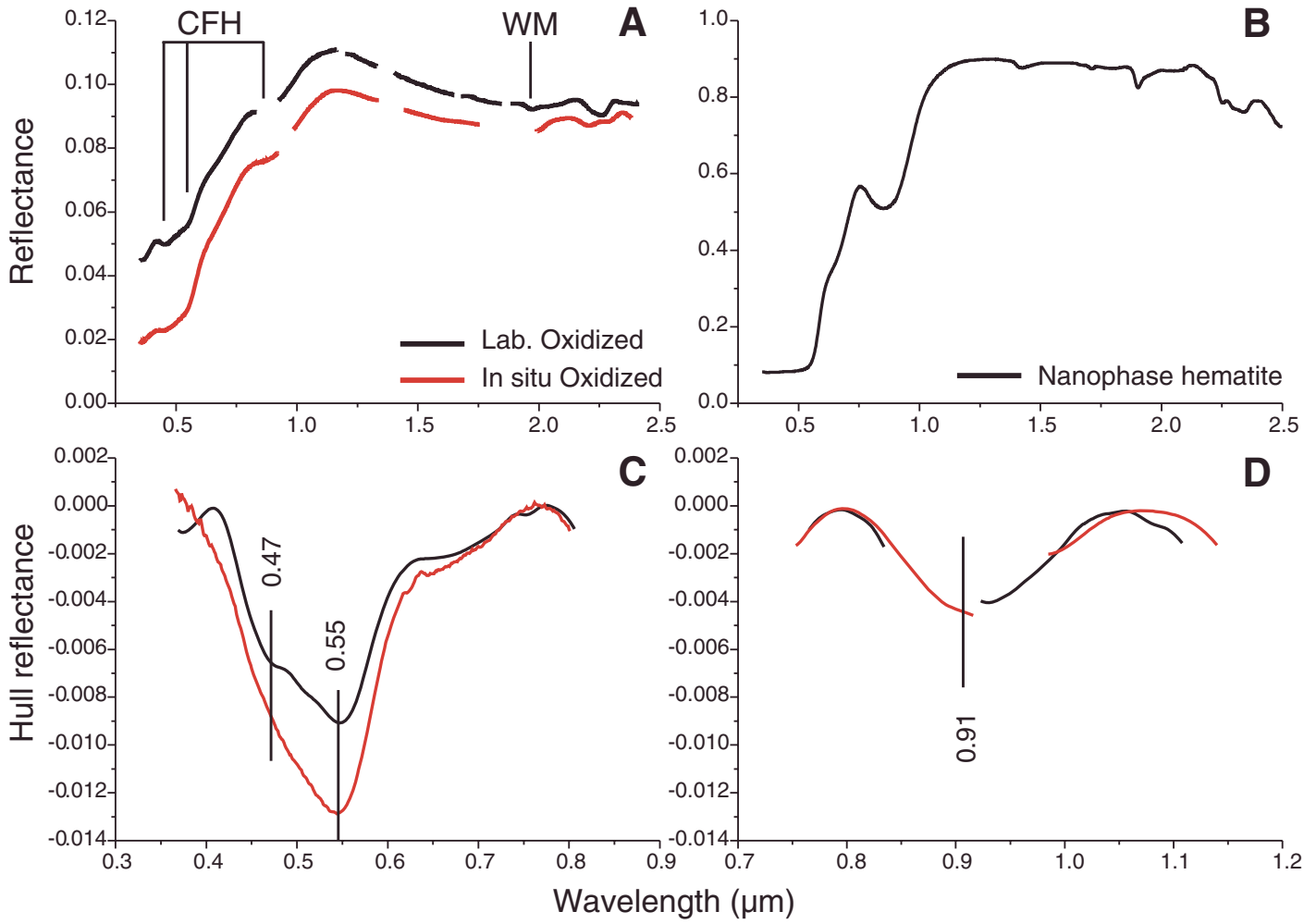

Figure 13. (A) Comparison between laboratory and field spectra of oxidized lava, proximal to the effusive centers, showing the Fe^{3+} absorption features characteristic of hematite. (B) Spectrum of hematite with <45 μm size, separated via filtering from oxidized lava samples. (C) and (D) Continuum-removed VIS (visible) spectra from A, showing individual absorption bands of the CFH spectral pattern. CFH and WM—spectral patterns (see Table 4 for explanation). See discussion in the text.

Currently operative spaceborne hyperspectral sensors show serious problems in resolving absorption features in both the VIS and NIR ranges, at least for surfaces characterized by a very low reflectance. More generally, low signal-to-noise ratios preclude the detection of rock spectral variability, which is critical for rock identification from remote data. New technologies are therefore required for successful mineralogical and lithological surveys.

ACKNOWLEDGMENTS

Field and Hyperion spectroscopic data acquisition was made in collaboration with INGV (Istituto Nazionale di Geofisica e Vulcanologia, Rome and Catania) and Valerio Tramutoli of the University of Catania. We are particularly thankful to Ted L. Roush for the critical reading of a first version of the manuscript. The useful comments and suggestions of two anonymous reviewers improved the manuscript. Financial support by ASI (Agenzia Spaziale Italiana) and MIUR (Ministero Italiano Università e Ricerca) is acknowledged.

REFERENCES CITED

Adams, J.B., Smith, M.O., and Johnson, P.E., 1986, Spectral mixture modelling: A new analysis of rock and soil types at the Viking Lander I site: Journal of Geophysical Research, v. 91, p. 8098–8112.

Andronico, D., Branca, S., Calvari, S., Burton, M.R., Caltabiano, T., Corsaro, R.A., Del Carlo, P., Garfi, G., Lodato, L., Miraglia, L., Neri, M., Pecora, E., Pompilio, M., Salerno, G., and Spampinato, L., 2005, A multi-disciplinary study of the 2002–03 Etna eruption: Insights into a complex plumbing system: Bulletin of Volcanology, v. 67, no. 4, p. 314–330, doi: 10.1007/s00445-004-0372-8.

Armienti, P., Clocchiatti, R., D'Orazio, M., Innocenti, F., Petrini, R., Pompilio, M., Tonarini, S., and Villari, L., 1994, The long-standing 1991–1993 Mount Etna eruption: Petrology and geochemistry of lavas: Acta Vulcanologica, v. 4, p. 15–28.

Barducci, A., De Cosmo, V., Marcoionni, P., and Pippi, I., 2004, ALISEO: A new stationery imaging interferometer, *in* Shen, S.S., and Lewis, P.E., eds., Proceedings, Imaging Spectrometry X: Denver, Colorado, The International Society for Optical Engineering (SPIE), v. 5546, p. 262–270.

Buongiorno, M.F., Musacchio, M., Merucci, L., Spinetti, C., Amici, S., Colini, L., Lombardo, V., Doumaz, F., Di Stefano, G., Pannaccione Apa, M.I., Caltabiano, T., Burton, M., Salerno, G., Bruno, N., Longo, V., Murè, F., Behncke, B., Neri, M., Giammanco, S., Badalamenti, B., Diliberto, I.S., Lotta, M., Madonia, P., Pugnaghi, S., Corradini, S., Relitti, M., Guerrieri, L., Lombroso, L., Boccolari, M., Teggi, S., Gobbi, G.P., Barnaba, F., Sgavetti, M., Pompilio, L., Tramutoli, V., Lanorte, V., Pergola, N., Marchese, F., Di Bello, G., Candela, O., Lindermeier, E., Haschberger, P., Tank, V., Oertel, D., Kick, H., Sanantonio, N., Mannarella, M., and Bugliolo, M.P., 2006, Etna 2003 field campaign: Calibration and validation of spaceborne and airborne instruments for volcanic applications: Quaderni di Geofisica, Istituto Nazionale di Geofisica e Vulcanologia (INGV) Publication (in press).

Burns, R.G., 1993, Mineralogical applications of crystal field theory: Cambridge, Cambridge University Press, 551 p.

Clark, R.N., and Roush, T.X., 1984, Reflectance spectroscopy: Quantitative analysis techniques for remote

sensing applications: Journal of Geophysical Research, v. 89, p. 6329–6340.

Clark, R.N., Swayze, G.A., Livo, K.E., Kokaly, R.F., Sutley, S.J., Dalton, J.B., McDougal, R.R., and Gent, C.A., 2003, Imaging spectroscopy: Earth and planetary remote sensing with the USGS Tetracorder and expert systems: Journal of Geophysical Research, v. 108, no. E12, p. 5131, doi: 10.1029/2002JE001847.

Cloutis, E.A., 2002, Pyroxene reflectance spectra: Minor absorption bands and effects of elemental substitutions: Journal of Geophysical Research, v. 107, p. 1–12.

Cloutis, E.A., and Gaffey, M.J., 1991, Pyroxene spectroscopy revisited: Spectral-compositional correlations and relationships to geothermometry: Journal of Geophysical Research, v. 96, p. 22,809–22,826.

Cristofolini, R., Menzies, M.A., Beccaluva, L., and Tindle, A., 1987, Petrological notes on the 1983 lavas at Mount Etna, Sicily, with reference to their REE and Sr-Nd isotope composition: Bulletin of Volcanology, v. 49, p. 599–607, doi: 10.1007/BF01079965.

Duke, F.E., 1994, Near infrared spectra of muscovite, Tschermak substitution, and metamorphic reaction progress: Implications for remote sensing: Geology, v. 22, p. 621–624, doi: 10.1130/0091-7613(1994)022<0621:NISOMT>2.3.CO;2.

Ferrari, M.C., Sgavetti, M., and Chiari, R., 1996, Thematic Mapper multispectral facies in prevalent carbonate strata of an area of Migiurtinia (northern Somalia): Analysis and interpretation: International Journal of Remote Sensing, v. 17, p. 111–130.

Grove, C.I., Hook, S.J., and Paylor, E.D., II, 1992, Laboratory reflectance spectra of 160 minerals, 0.4 to 2.5 micrometers: Jet Propulsion Laboratory Publication 92-2, 406 p.

Guidotti, C.V., and Sassi, F.P., 1976, Muscovite as a petrogenetic indicator mineral in pelitic schists: Neues Jahrbuch für Mineralogie-Abhandlungen, v. 127, p. 97–142.

Hapke, B., 2001, Space weathering from Mercury to the asteroid belt: Journal of Geophysical Research, v. 106, p. 10,039–10,073, doi: 10.1029/2000JE001338.

Harloff, J., and Arnold, G., 2001, Near-infrared reflectance spectroscopy of bulk analog materials for planetary crust: Planetary and Space Science, v. 49, p. 191–211, doi: 10.1016/S0032-0633(00)00132-X.

Hawthorne, F.C., and Waychunas, G.A., 1988, Spectrum-fitting methods, *in* Hawthorne, F.C., ed., Spectroscopic methods in mineralogy and geology: Reviews in Mineralogy, v. 18, p. 63–98.

Hunt, G.R., 1980, Electromagnetic radiation: The communication link in remote sensing, *in* Siegal, B.S., and Gillespie, A.R., eds., Remote sensing in geology: New York, John Wiley & Sons, p. 5–45.

King, T.V.V., and Ridley, W.L., 1987, Relation of the spectroscopic reflectance of olivine to mineral chemistry and some remote sensing implications: Journal of Geophysical Research, v. 92, p. 11,457–11,469.

Kruse, F.A., Calvin, W.M., and Seznec, O., 1988, Automated extraction of absorption features from airborne visible/infrared imaging spectrometer (AVIRIS) and geophysical and environmental research imaging spectrometer (GERIS) data, *in* Proceedings, Airborne Visible/Infrared Imaging Spectrometer (AVIRIS) performance evaluation workshop: Jet Propulsion Laboratory Publication 88-38, p. 62–75.

Kruse, F.A., Lefkoff, A.B., Boardman, J.W., Heidebrecht, K.B., Shapiro, A.T., Barloon, J.P., and Goetz, A.F.H., 1993, The spectral image processing system (SIPS)—Interactive visualization and analysis of imaging spectrometer data: Remote Sensing of Environment, v. 44, p. 145–163, doi: 10.1016/0034-4257(93)90013-N.

Longhi, I., Mazzoli, C., and Sgavetti, M., 2000, Metamorphic grade in siliceous muscovite-bearing rocks through laboratory reflectance and imaging spectroscopy: Terra Nova, v. 12, p. 21–27, doi: 10.1046/j.1365-3121.2000.00264.x.

Longhi, I., Sgavetti, M., Chiari, R., and Mazzoli, C., 2001, Spectral analysis and classification of metamorphic rocks from laboratory reflectance and transmittance spectra in the 0.4–2.5 µm and 2.5–25 µm regions: A tool for hyperspectral data interpretation: International Journal of Remote Sensing, v. 22, p. 3763–3782, doi: 10.1080/01431160010006980.

Longhi, I., Sgavetti, M., Pompilio, L., and Meli, S., 2004, Complex spectral interactions of different minerals and textures in Mars terrestrial analogues: Some examples: Planetary and Space Science, v. 52, p. 141–147, doi: 10.1016/j.pss.2003.08.025.

Mazer, A.S., Martin, M., Lee, M., and Solomon, J.E., 1988, Image processing software for imaging spectroscopy data analysis: Remote Sensing of Environment, v. 24, p. 201–210, doi: 10.1016/0034-4257(88)90012-0.

McSween H.Y., Grove, T.L., and Wyatt, M.B., 2003, Constraints on the composition and petrogenesis of the Martian crust: Journal of Geophysical Research, v. 108, no. E12, p. 5135, doi: 10.1029/2003JE002175,2003.

Meigs, A.D., Otten, L.J., III, Cherezova, T.Y., Rafert, B., and Sellar, R.G., 1997, LWIR and MWIR ultraspectral Fourier transform imager, *in* Fujisada, H., ed., Proceedings, Sensors, systems, and next generation satellite: London, The International Society for Optical Engineering (SPIE), v. 3221, p. 421–428.

Moine, B., 1974, Charactères de sedimentation et de métamorphisme des series Précambriennes épizonales à catazonales du centre de Madagascar (Région d'Ambatofinandrahana) [Ph.D. thesis]: Annales de l'Ecole Nationale Supérieure de Géologie Appliquée et de Prospection Minière du Centre de Recherche Pétrographiques et Géochimiques (C.N.R.S.) et des Laboratoires dès Sciences de la Terre de l'Université: Mémoires de Sciénces de la Terre, v. 31, 293 p.

Mustard, J.F., Poulet, F., Gendrin, A., Bibring, J.P., Langevin, Y., Gondet, B., Mangold, N., Bellucci, G., and Altieri, F., 2005, Olivine and pyroxene diversity in the crust of Mars: Science, v. 307, p. 1594–1597, doi: 10.1126/science.1109098.

Pompilio, L., 2005a, Reflectance spectroscopy (VNIR) of igneous rocks: Characterization of the Bjerkreim-Sokndal cumulates [Ph.D. thesis]: Parma, Italy, Parma University, 248 p.

Pompilio, L., 2005b, Reflectance spectroscopy (VNIR) of igneous rocks: Characterization of the Bjerkreim-Sokndal cumulates: European Journal of Mineralogy, supplement, Plinius, v. 31, p. 203–209.

Post, J.L., and Noble, P.N., 1993, The near-infrared combination band frequencies of dioctahedral smectites, micas, and illites: Clay and Clay Minerals, v. 41, p. 639–644.

Romano, R., 1982, Succession of the volcanic activity in the Etnean area: Memorie della Società Geologica Italiana, v. 23, p. 27–48.

Sgavetti, M., Ferrari, M.C., Chiari, R., Fantozzi, P.L., and Longhi, I., 1995, Stratigraphic correlation by integrated photostratigraphy and remote sensing multispectral data: An example from Jurassic to Eocene strata in an area of northern Somalia: Bulletin of the American Association of Petroleum Geologists, v. 79, p. 1571–1589.

Sgavetti, M., Tramutoli, V., Pompilio, L., and Longhi, I., 2003, Field spectroscopy on Mount Etna, *in* Blanco A., Dotto, E., and Orofino, V., eds., Proceedings, Fifth Italian Meeting of Planetary Science: Lecce, Italy, University of Lecce, p. 246–252.

Sgavetti, M., Longhi, I., Meli, S., and Pompilio, L., 2006, Accuracy in mineral identification: Image spectral and spatial resolution and mineral spectral properties: Annals of Geophysics, v. 49, no. 1 (in press).

Straub, D.W., Burns, R.G., and Pratt, S.F., 1991, Spectral signature of oxidized pyroxenes: Implications to remote sensing of terrestrial planets: Journal of Geophysical Research, v. 96, p. 18,819–18,830.

Sunshine, J.M., Pieters, C.M., and Pratt, S.F., 1990, Deconvolution of mineral absorption bands: An improved approach: Journal of Geophysical Research, v. 95, p. 6955–6966.

Swayze, G., Clark, R.N., Kruse, F., Sutley, S., and Gallagher, A., 1992, Ground truthing AVIRIS mineral-mapping at Cuprite, Nevada, *in* Proceedings, Third Annual JPL Airborne Geoscience Workshop: Jet Propulsion Laboratory Publication 92-14, p. 47–49.

Wilcox, B.B., Lucey, P.G., and Gillis, J.J., 2005, Mapping ion in the lunar mare: An improved approach: Journal of Geophysical Research, v. 110, p. E11001, doi: 10.1029/2005JE002512.

Manuscript Received by the Society 12 October 2005
Revised Manuscript Received 3 March 2006
Manuscript Accepted 17 March 2006